Sensitivity of mountain wave drag estimates on separation methods and proposed improvements

Zuzana Procházková,[a] Christopher G. Kruse,[b] M. Joan Alexander,[b] Lars Hoffmann,[c] Julio T. Bacmeister,[d] Laura Holt,[b] Corwin Wright,[f] Kaoru Sato,[g] Sonja Gisinger,[h] Manfred Ern,[i] Markus Geldenhuys,[i] Peter Preusse,[i] and Petr Šácha,[a,j]

[a] *Department of Atmospheric Physics, Faculty of Mathematics and Physics, Charles University, Prague, Czech Republic*

[b] *NorthWest Research Associates, Boulder, Colorado, USA*

[c] *Jülich Supercomputing Centre, Forschungszentrum Jülich, Jülich, Germany*

[d] *ECMWF, Reading, UK*

[e] *Climate and Global Dynamics Laboratory, NCAR, Boulder, Colorado, USA*

[f] *Centre for Space, Atmospheric and Oceanic Science, University of Bath, Bath, UK*

[g] *Department of Earth and Planetary Science, University of Tokyo, Tokyo, Japan*

[h] *Institute of Atmospheric Physics, Deutsches Zentrum für Luft- und Raumfahrt, Oberpfaffenhofen, Germany*

[i] *Institut für Energie- und Klimaforschung - Stratosphäre (IEK-7), Forschungszentrum Jülich, Jülich, Germany*

[j] *Institute of Meteorology and Climatology, University of Natural Resources and Life Sciences, Vienna (BOKU)*

Corresponding author: Zuzana Procházková, prochazkova@karlin.mff.cuni.cz

ABSTRACT: Internal gravity waves (GWs) are ubiquitous in the atmosphere, making significant contributions to the mesoscale motions. Since the majority of their spectrum is unresolved in global circulation models, their effects need to be parameterized. In recent decades GWs have been increasingly studied in high-resolution simulations, which, unlike direct observations, allow us to explore full spatio-temporal variations of the resolved wave field. In our study we analyze and refine a traditional method for GW analysis in a high-resolution simulation on a regional domain around the Drake Passage. We show that GW momentum drag estimates based on the Gaussian high-pass filter method applied to separate GW perturbations from the background are sensitive to the choice of a cutoff parameter. The impact of the cutoff parameter is higher for horizontal fluxes of horizontal momentum, which indicates higher sensitivity for horizontally propagating waves. Two modified methods, which choose the parameter value from spectral information, are proposed. The dynamically determined cutoff is mostly higher than the traditional cutoff values around 500 km, leading to larger GW fluxes and drag, and varies with time and altitude. The differences between the traditional and the modified methods are especially pronounced during events with significant drag contributions from horizontal momentum fluxes.

SIGNIFICANCE STATEMENT: In this study, we highlight that the analysis of gravity wave activity from high-resolution datasets is a complex task with a pronounced sensitivity to the methodology, and we propose modified versions of a classical statistical gravity wave detection method enhanced by the spectral information. Although no optimal methodology exists to date, we show that the modified methods improve the accuracy of the gravity wave activity estimates, especially when oblique propagation plays a role.

1. Introduction

Internal gravity waves (GWs) manifest themselves in the flow as oscillations supported by the buoyancy force within the fluid (Holton 2004). One of their crucial properties is the variety of temporal and spatial scales on which they emerge. Horizontal wavelengths of GWs range from thousands to a few kilometres (Fritts and Alexander 2003), being increasingly affected by rotation at the upper wavelength bound (e.g. inertia-GWs) and by nonhydrostatic effects with dominating vertical velocity component at the lower bound. They dominate the mesoscale wave spectrum (wavelengths in the order of 10 - 1000 km) in the middle atmosphere (Andrews et al. 1987), but they also impact the synoptic (Achatz et al. 2017) and planetary scale circulations (Andrews et al. 1987) and can also directly influence the surface weather conditions including extreme weather events (Damiens et al. 2018). Furthermore, they impact the mesospheric circulation and are responsible for the upper mesospheric wind reversal, the cold summer mesopause and warm winter stratopause (Dunkerton 1978; Lindzen 1981).

The fact that GWs exist and exert influence across a wide range of scales presents a challenge for numerical climate atmospheric models, as a significant portion of the GW spectrum is smaller than the scale of the computational grid. Hence, momentum deposition and other possible effects of the unresolved part of the spectrum have to be parameterized. GW parameterization schemes rely on various simplifications of the sourcing, propagation and dissipation processes and employ several tunable parameters, as reviewed recently in Plougonven et al. (2020). Given the importance of GW parameterizations for model circulation and dynamics (Polichtchouk et al. 2018; Van Niekerk et al. 2018a; Eichinger et al. 2020; Sacha et al. 2021), this brings an undesirable level of uncertainty to the simulations.

Constraining the tunable parameters is complicated, because this requires general knowledge of GW global distribution, wavelengths, frequencies, momentum fluxes, etc. (Alexander et al. 2010), which cannot be to date derived from global scale (satellite) observations. That said, increasing attention is being paid to high-resolution numerical models that are becoming capable of simulating the life-cycle of a broad spectrum GWs (Smith et al. 2007; Kruse et al. 2022). For deriving momentum flux (MF) and GW drag (GWD) estimates from such complex data sets (often in a bounded domain), Reynolds decomposition is usually applied and some type of a GW separation method has to be used.

Many approaches exist to date ranging from theoretical approaches based on various forms of balanced-unbalanced flow separation (Mirzaei et al. 2017; Gaßmann 2019) including potential vorticity inversion techniques (Viúdez 2012), cosine (Denis et al. 2002), modal (Stephan et al. 2021, 2022) or Helmholtz (Bühler et al. 2014; Lindborg 2015) decomposition or the Transformed Eulerian mean framework (Gupta et al. 2021) or its generalization (Kinoshita and Sato 2013), to approaches that involve various forms of spectral methods and transforms (Wright and Gille 2013; Preusse et al. 2014; Schoon and Zülicke 2018; Kruse and Smith 2015; Dörnbrack 2021). In our study, we apply two methods that have been used in the literature before for GW separation and consequent momentum flux evaluation in a limited model domain, that allow easy application and straightforward GWD computation, the S3D method (Lehmann et al. 2012) and high-pass filtering method of Kruse and Smith (2015). We demonstrate the sensitivity of the resulting GWD estimates on the method and propose two modifications of the high-pass filtering method based on underlying spectral analysis that can mitigate the uncertainty of GWD estimates connected with the subjective choice of the cutoff wavelength in the filter.

In Section 2 of the paper, we first review the theory of the high-pass filter method for GW separation, the kinetic energy spectrum calculation and S3D method and we describe the algorithms of the modified methods. In Section 3 the analysed dataset is described together with the methodology for drag estimates. In Section 4, we first show the kinetic energy spectrum of the combined data (Section 4a) and the uncertainty of the standard high-pass filter method (Section 4b). The resulting drag estimates from different methods are compared in Section 4c. Finally, in Section 4d, the distribution of the error among the individual components of GWD is studied. The paper ends with discussion and concluding remarks in Section 5.

2. Methodology

a. High-pass Filter Method

We implement the high-pass filter method introduced in Kruse and Smith (2015) on a Cartesian domain with constant 3-km horizontal resolution. The method uses a Gaussian filter, which modulates simulated fields of velocity components by convolution with a Gaussian function (Gonzalez and Woods 2008).

In practice, the fast Fourier transform (FFT) algorithm is used instead of convolution. The high-pass filter can be then formulated using the response function

$$\hat{r}_{hp}(k,l) = 1 - \mathrm{e}^{-\left(k^2+l^2\right)\frac{L^2}{4\pi^2}}, \tag{1}$$

where k and l are zonal and meridional wavenumbers, respectively, and L is a cutoff parameter corresponding to the width of the Gaussian function in the Fourier/wavenumber space. The Fourier coefficients are multiplied by the response function and the inverse FFT is applied to the product, removing the large-scale patterns and leaving the small-scale perturbations intact.

The exponential function in Eq. (1) is, up to a scaling factor, a Gaussian function with the variance $\sigma^2 = 2\pi^2/L^2$. As 95 % of the filtered waves will have wavenumber smaller than $2\sigma = 2\pi\sqrt{2}/L$, the wavelengths $\tilde{\lambda}$ that are retained fulfil

$$\tilde{\lambda} < \frac{L}{\sqrt{2}}. \tag{2}$$

After choosing an appropriate value for the parameter L, the perturbations with the wavelengths $\tilde{\lambda}$ that are retained by the application of the high-pass response function in Eq. (1) are commonly assumed to consist exclusively of GWs.

The periodization procedures applied before the FFT step will be discussed in Section 2c.

b. Horizontal Energy Spectrum

As the width of the spectrum of GWs on a local domain is variable (see Section 4c), we aim to modify the high-pass filter method introduced above, so that the cutoff parameter reflects the actual range of GW modes. To this end, we study the specific horizontal kinetic energy

spectrum, which is computed at a given altitude as a sum of energies for individual horizontal modes

$$E^z_{k,l} = \frac{1}{2N^2}\left(\hat{u}_{k,l}\hat{u}^*_{k,l} + \hat{v}_{k,l}\hat{v}^*_{k,l}\right), \tag{3}$$

where $\hat{u}_{k,l}$ and $\hat{v}_{k,l}$ are horizontal Fourier transforms of zonal and meridional velocities and N is number of points in both horizontal directions.

Making explicit the divergent and vortical properties of the flow, the previous formula can be alternatively written in the form

$$E^z_{k,l} = \frac{1}{2N^2}\frac{\hat{\zeta}^z_{k,l}(\hat{\zeta}^z_{k,l})^* + \hat{\delta}^z_{k,l}(\hat{\delta}^z_{k,l})^*}{\left(\frac{2\pi}{N\Delta x}\right)^2\left(k^2+l^2\right)}, \tag{4}$$

where $\hat{\zeta}^z_{k,l}$ and $\hat{\delta}^z_{k,l}$ are horizontal Fourier transforms of horizontal vorticity and divergence. The first summand in the expression can be viewed as the rotational part of the spectrum and the second one as the divergent part.

The 2D spectrum described by Eq. (3) or (4) can be summed up to obtain a 1D spectrum. The exact procedure of the spectrum computation and the derivation of the second formula is described in detail in Appendix A.

By the theory, we can expect the horizontal kinetic energy spectrum being proportional to $K^{-5/3}$ for GW-dominated mesoscale (Menchaca and Durran 2019) and proportional to K^{-3} for larger scales (Geller and Gong 2010; Vallis 2017; Gage and Nastrom 1986). The latter dependence, based on the quasi two-dimensional theory of turbulence at large scales, is related to the enstrophy. Such theoretical proportionalities were repeatedly confirmed by observational studies (Nastrom and Gage 1985; Lindborg 1999) and from high-resolution simulations (Blažica et al. 2013; Skamarock 2004).

c. Periodization Method

For computation of the horizontal energy spectrum, we used discrete Fourier transform (DFT). However, DFT assumes that the data are periodic, which is not true for a local domain. Removal of these aperiodicities is essential to get a correct, unbiased spectrum (Bierdel et al. 2012).

There are different approaches to this problem. The method we implemented for the spectrum computation is a detrending method presented by Errico (1985). It is based on subtracting the linear trend from each row and column of the data, where the slope is computed using the boundary values only. If the data values are denoted by $b_{i,j}$, $i = 1, \ldots, N$, $j = 1, \ldots, M$, we can write the slope of a line connecting the first and the last element in j-th column as

$$s_j = \frac{b_{N,j} - b_{1,j}}{N-1}. \tag{5}$$

The values along the line are then modified by a line with the slope s_j so that the resulting column is periodic,

$$b'_{i,j} = b_{i,j} - i s_j + \frac{1}{2}\frac{N+1}{N-1}\left(b_{N,j} - b_{1,j}\right). \tag{6}$$

The same procedure is applied also on rows.

The drawback of this method is that it creates artificial small-scale structures (Denis et al. 2002). Hence, we only apply the method to obtain the horizontal kinetic energy spectrum and derived spectral characteristics. We do not use it for the high-pass filtering with a fixed cutoff parameter. In this case, we only subtract global linear trend in the data (evaluated by fitting a plane to the data). The boundary effects are assumed to be small (Kruse and Smith 2015), but we note that especially for larger cutoff values, the effect of non-periodicity can extend further in the domain and project to our drag estimates. This effect can be mitigated by a replacement of DFT by discrete cosine transform (Denis et al. 2002). In our case the application of the discrete cosine transform resulted in negligible differences (see Fig. S1 in the Supplementary Material) with the DFT based results, confirming that the boundary effects are small in our study. For consistency with Kruse et al. (2022) we base our method on DFT.

d. Methods for Dynamical Cutoff Selection

Following the changepoint analysis of Burgess et al. (2013), we propose two modifications of the Gaussian high-pass filter method, in which we use horizontal kinetic energy spectra to estimate an optimal cutoff value variable with time and altitude. To get an integral information on GWs from the spectra, the spectra are smoothed by moving average with the length of 15 hours before applying any of the statistics described below.

1) Spectral Slope Method

The first modification of the high-pass filter method evaluates the cutoff parameter from the slopes in the energy spectrum.

Based on the characteristic slopes, we can identify three parts of the spectrum - synoptic, mesoscale and for the shortest wavelengths, starting from the so-called effective resolution, we observe a steep descent of the kinetic energy. The exact value of the effective resolution of a model depends on a set of factors (horizontal and vertical resolution, numerical dissipation, filtering, etc.). Below this threshold specific GW modes can still be partially resolved, but as we go to smaller wavelengths, an increasing part of the modes are unresolved.

By assuming that GWs dominate the mesoscale part of the spectrum in our domain, we choose the cutoff using the wavelength at which the spectrum slope changes from $-5/3$ (the exact connection of the wavelength to the cutoff value is through Eq. (2)).

The detection of the change-of-slope wavelength involves some non-trivial technical aspects: The algorithm subdivides the range of wavelengths in the logarithmic spectrum plot into two sequences, the first sequence well fitted by a line with an arbitrary slope and the second sequence well fitted by a line with the slope -5/3. The second sequence is then considered the range of GWs. The algorithm constructs the sequences iteratively, always adding the neighboring wavelength into the sequence into which its neighboring wavelength fits better. The error metric used for comparing the quality of the sequences is their line fitting error. The sequences are initialized by the wavelength corresponding to the effective resolution, which is assumed to lie in the GW range, and by the longest wavelength present, respectively, which is assumed to lie outside the GW range. The full algorithm is described in Appendix C.

This process described above is applied on each of the smoothed spectra, resulting in a cutoff length for each time step (apart from the initial and final time steps that are discarded during the smoothing).

Further on, we will refer to the high-pass filter method that uses cutoff specified by this algorithm as the spectral slope method.

2) Divergence Dominated Method

According to Saujani and Shepherd (2006), a simple way to distinguish between balanced and unbalanced flow exists by comparing the relative magnitudes of divergent and rotational flow. For balanced dynamics, the divergent part is much weaker than the rotational motion and vice-versa. This motivates us to determine the cut-off based on the intersection of divergent and rotational spectra following Burgess et al. (2013), assuming that GWs (although partly also having the rotational component) dominate the spectrum, where the divergent part dominates. Detection of the wavelength at which the divergent spectrum equals the rotational is not straightforward, as there can be multiple intersections of the spectra. The applied algorithm therefore considers also distances between individual intersections and chooses a maximal wavelength of a divergence-dominated interval such that there is no divergence-dominated wavelength interval for larger wavelengths that would be longer than the vorticity-dominated interval for smaller wavelengths.

We will refer to the high-pass filter method using cutoff specified at each time step (again apart from the initial and final time steps because of spectrum smoothing) by this algorithm as the divergence dominated method.

e. S3D Method

For comparison, we also derive GWD estimates using the widely used S3D method for GW detection (Lehmann et al. 2012; Stephan et al. 2019; Preusse et al. 2014; Ern et al. 2017; Krisch et al. 2017; Strube et al. 2021; Krasauskas et al. 2022).

In the applied settings, temperature data are analyzed. Separation into background and GWs is performed by a FFT high-pass filter retaining all spectral components corresponding to wavelengths shorter than 500 km. The whole volume is then divided into overlapping cuboids of 100 km x 100 km x 11 km (zonal x meridional x vertical direction) with cuboid centres every 0.39°in zonal and meridional direction and every 1 km in vertical direction. In the cuboids sinusoidal fits of the most and second significant wave component are performed resulting in the 3D wave vector, amplitude and phase for both wave components (Lehmann et al. 2012). Fit results where the wavelengths exceed 3 times the vertical or 3.5 times the horizontal cuboid size are suppressed in the fitting by adding a penalty to the χ^2-values used in the fitting and, where still present,

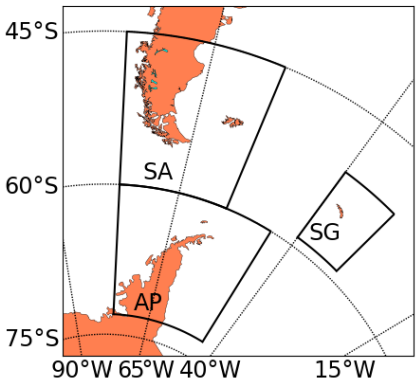

FIG. 1. Horizontal domain with marked subdomains Southern Andes (SA), Antarctic Peninsula (AP) and South Georgia (SG).

removed afterwards. According to Ern et al. (2004) GW momentum flux is then determined from the wave parameters.

3. Data and Implementation

We use data from a hindcast simulation of Weather Research and Forecasting (WRF) Model (Skamarock et al. 2019b) on a local domain covering parts of Southern America, Antarctica and the south-east of the Atlantic Ocean described in Kruse et al. (2022). The GW filtering is applied on the full simulation domain displayed in Fig. 1, described using the simplified Lambert Conformal map projection. Following Kruse et al. (2022), we subsequently divide the domain into three GW hotspots, see Fig. 1, Southern Andes (SA), Antarctic Peninsula (AP) and South Georgia (SG), where we estimate the mountain wave drag (MWD).

After the initialization at 12 UTC on 8th October 2010, the model was integrated for 11 days with the output frequency of 15 minutes. The simulation was guided by 6-hourly operational IFS analyses via initial and boundary conditions. The model uses hybrid sigma-pressure vertical coordinate, but for the computations, the data (pressure, potential temperature and velocity components fields) were first linearly interpolated on equidistant vertical levels of geopotential height with 1 km spacing. To make the computation of horizontal derivatives easier, after the filtering, we interpolate the data also horizontally from the simplified Lambert Conformal map projection of the model to a regular grid defined by values of latitude and longitude with the same horizontal resolution as the original

data (the average distance between points along parallels and meridians is set to be 3 km). This regridding is performed using the ESMF_regridding package in NCAR Command Language (NCL 2019).

The scripts and algorithms were implemented partly in Python and partly in NCL. They were parallelized using the Python multiprocessing package and the program GNU parallel (Tange et al. 2011). The diagnostic algorithms are accessible through the link in Procházková (2021).

Gravity Wave Drag

As the wind blows against a mountainside, it excites mountain waves (MWs), and it exerts a pressure force on the mountain surface. In accordance with Newton's third law, this gives rise to a drag force acting in the opposite direction on the air, which is called mountain drag. The mountain drag is deposited not only locally in the vicinity of the mountain, but is also propagated by the MWs in a form of MFs to the free atmosphere, where the mountain wave drag (MWD, a subset of GWD) is deposited at the level of their dissipation (Kruse and Smith 2018), i.e. resulting in MF divergence. Estimating the drag exerted by GWs higher up from the surface is a complex task for which various approximations exist. Here we follow the method used by Kruse et al. (2022) and Kruse and Smith (2015) based on spatial averaging across the MW source regions. The hotspot regions follow Kruse et al. (2022) and have been defined to contain as much of the wave activity from individual sources as possible, while minimizing the influence of lateral propagation of large-scale waves through the subdomains. The assumption on the area of the subdomains is that $\overline{u'} = 0$, where $\overline{(\cdot)}$ is an average over a 2D domain A and u' denotes wave perturbation, while the synoptic scale variables do not vary considerably over the subdomains. Obviously, the choice of the area A can never be optimal, which can introduce some uncertainty. Its quantification is however out of the scope of the current manuscript and we follow the choice of the subdomains from Kruse and Smith (2015) (the horizontal dimensions of the subdomains are approximately 1700 x 1700 km^2 for SA, 1800 x 1400 km^2 for AP and 700 x 900 km^2 for SG, Fig. 1).

The resulting MFs form a rank-two tensor, whose divergence represents the MWD vector. In spherical coordinates, defined by the radial coordinate r, latitude φ and longitude λ, MWD components are computed as (taking into account the shallow atmosphere approximation implicit

to the WRF model to substitute the radius r by the radius of Earth r_e):

$$MWD_x = MWD_{xx} + MWD_{yx} + MWD_{zx}, \tag{7a}$$

$$MWD_{xx} \approx -\frac{r_e}{A}\left[\int u'^2 \,\mathrm{d}\varphi\right]_{\lambda_1}^{\lambda_2}, \tag{7b}$$

$$MWD_{yx} \approx -\frac{r_e}{A}\left[\int u'v' \cos\varphi \,\mathrm{d}\lambda\right]_{\varphi_1}^{\varphi_2} - \frac{r_e}{A}\iint u'v' \sin\varphi \,\mathrm{d}\lambda \,\mathrm{d}\varphi, \tag{7c}$$

$$MWD_{zx} \approx -\frac{r_e^2}{A}\frac{1}{\hat{\rho}}\partial_r \iint \hat{\rho} u'w' \cos\varphi \,\mathrm{d}\lambda \,\mathrm{d}\varphi, \tag{7d}$$

$$MWD_y = MWD_{xy} + MWD_{yy} + MWD_{zy}, \tag{7e}$$

$$MWD_{xy} \approx -\frac{r_e}{A}\left[\int u'v' \,\mathrm{d}\varphi\right]_{\lambda_1}^{\lambda_2}, \tag{7f}$$

$$MWD_{yy} \approx -\frac{r_e}{A}\left[\int v'^2 \cos\varphi \,\mathrm{d}\lambda\right]_{\varphi_1}^{\varphi_2} - \frac{r_e}{A}\iint v'^2 \sin\varphi \,\mathrm{d}\lambda \,\mathrm{d}\varphi, \tag{7g}$$

$$MWD_{zy} \approx -\frac{r_e^2}{A}\frac{1}{\hat{\rho}}\partial_r \iint \hat{\rho} v'w' \cos\varphi \,\mathrm{d}\lambda \,\mathrm{d}\varphi, \tag{7h}$$

where the dashed quantities u', v' and w' are the perturbation components of flow velocity and $\hat{\rho}$ is the area average of the density. The area A bounded by latitudes φ_1 and φ_2 and longitudes λ_1 and λ_2 is given by

$$A = \iint r^2 \cos\varphi \,\mathrm{d}\lambda \,\mathrm{d}\varphi \approx r_e^2 \left(\lambda_2 - \lambda_1\right)\left(\sin\varphi_1 - \sin\varphi_2\right). \tag{8}$$

The complete derivation of analogous formula for Cartesian coordinates is shown in Appendix B. The additional terms that appear in the equations for the spherical coordinates (compared to the equations in Cartesian coordinates) result from the differentiation of geometric factors such as $\sin\varphi$.

For the S3D method, only the vertical derivatives of the vertical fluxes of the horizontal momentum are evaluated from temperature amplitudes using the approach described e.g. in Ern et al. (2017).

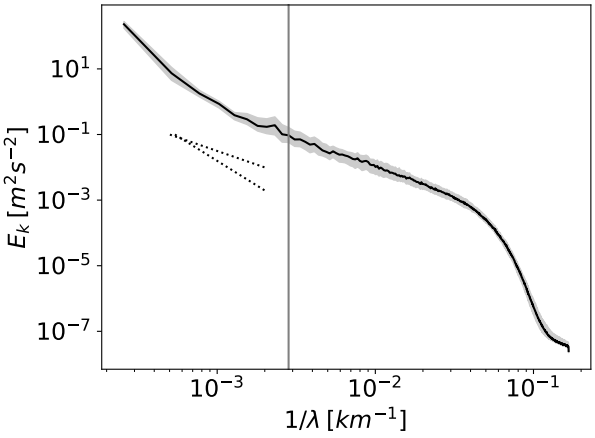

FIG. 2. Horizontal spectrum of specific horizontal kinetic energy at 20 km. Plot displays the median spectrum over the time period, the filled region denotes the range between the lower and upper quartile. Vertical line denotes the wavelength of about 354 km that corresponds to the cutoff 500 km. The dotted lines display the theoretical slopes -3 and -5/3.

4. Results

a. Broad Spectrum of GWs

First, we show the mean spectrum of horizontal kinetic energy for the altitude of 20 km in Fig. 2, evaluated for the whole WRF domain. To guide the reader's eye, the theoretical slopes of -5/3, where we expect GWs to dominate the wave field, and -3 are illustrated by dashed curves below the spectral line. The spectrum follows approximately the -5/3 slope for horizontal wavelengths from approximately 25 km up to about 800 km in an average over the simulation period. By eye, the hypothetical upper bound for the GW dominated spectrum given by the spectral slope approach is larger than the wavelength of approximately 354 km, corresponding to the cutoff length 500 km (denoted in Fig. 2 by vertical line), used in the high-pass filter method by Kruse et al. (2022). The range up to which the spectrum follows the slope -5/3 is dependent on the altitude, which will be studied in more detail in Section 4c. For example, at the altitude of 40 km, the upper bound of the GW dominated spectrum is higher than 1000 km in average (plot of the mean spectrum of horizontal kinetic energy for 40 km is shown in the Supplementary Material in Fig. S2).

The spectrum with its shape also varies in time. To illustrate this, we show the time evolution of a local spectral slope between neighbouring wave modes for the altitude of 20 km in Fig. 3

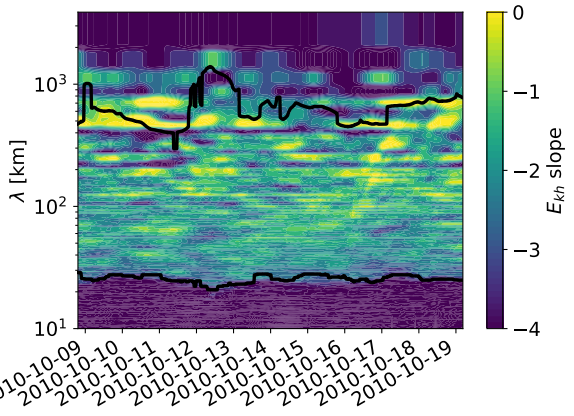

310 FIG. 3. Approximation of local slopes in the horizontal spectrum of specific horizontal kinetic energy at 20 km
311 (colours). The black lines visualise the time evolution of the effective resolution and of the upper bound for GWs
312 (described in Section 2d).

299 (a similar plot for 40 km is in the Supplementary Material in Fig. S4). The presented local slopes
300 in the figure, evaluated from adjacent data values, were calculated from immediate specific hor-
301 izontal energy spectra after a noise reduction by the 15-point Savitzky–Golay filter (Ostertagova
302 and Ostertag 2016). With a suitably chosen colour scale, we can see that the GW dominated part
303 of the spectrum can be well distinguished during the whole simulation. The lower bound corre-
304 sponding to the effective resolution is especially sharp and stable. However, the exact identification
305 of the upper bound is more tricky (the developed algorithm is described in Subsection 4c), because
306 at this region, the spectrum is often dominated by isolated peaks that are identifiable by zero slopes
307 (yellow colour). Those peaks are often missed by the algorithm and also it cannot be said with
308 certainty that those peaks belong to GW modes. This brings an inevitable uncertainty, however
309 small, to our MF and MWD estimates presented in Subsections 4c and 4d.

313 Next, we show in Fig. 4 the rotational and divergent components corresponding to spectrum of
314 horizontal kinetic energy at the altitude of 20 km (Fig. S2 in Supplementary material for 40 km). As
315 discussed in Section 2c, we can see the domination of the divergence component in the mesoscale
316 part of the spectrum and the prevalence of the rotational component for longer wavelengths. Again,
317 note that the median cut-off wavelength determined by the divergence dominated method is much
318 larger than the wavelength corresponding to the 500 km cut-off, which is denoted by the grey
319 vertical line in the figure.

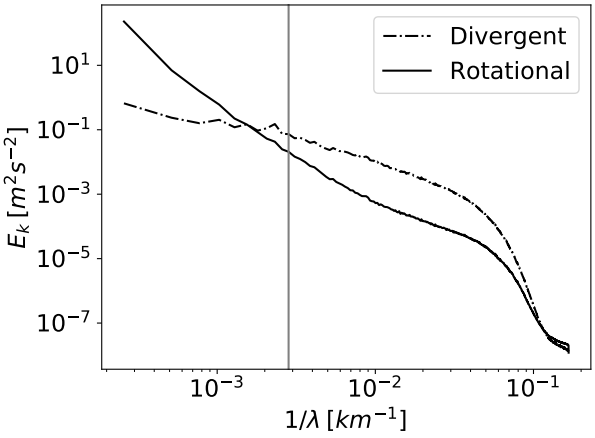

FIG. 4. Decomposition of horizontal spectrum of specific horizontal kinetic energy at 20 km into divergent and rotational part. Plot displays the median rotational and divergent part of the spectrum over the time period. Vertical line denotes the wavelength of about 354 km that corresponds to the cutoff 500 km.

b. Sensitivity of the MWD Estimates to the Cutoff

Further motivation for a modification of the traditional high-pass filter method used for GW separation is its sensitivity to the choice of the cutoff length, which is demonstrated in Fig. 5 for the altitude of 20 km (for 40 km, it is shown in the Supplementary Material in Fig. S5). To obtain these figures, we computed multiple MWD estimates following Section 3 from the high-pass filtered data with constant cutoff, but for multiple cutoff choices ranging between 250 km and 1550 km with a step size of 50 km. From the set of multiple MWD estimates for each time and domain, the derivative with respect to the cutoff length was computed using finite differences. For an easier interpretation of significance of the sensitivity, the derivatives are scaled by the median of the absolute value of the MWD component over the time and cutoff length, i.e. the sensitivity is plotted as:

$$\frac{1}{\left(med_{t,L}\left(|MWD|\right)\right)(z)}\frac{\mathrm{d}MWD\,(t,L,z)}{\mathrm{d}L}. \tag{9}$$

The high-pass filter method relies on the existence of a clear separation of the mesoscale modes from synoptic scale modes, i.e. the existence of a spectral band where the MWD and MF estimates do not significantly depend on the cutoff length is assumed. In Figure 5, we show the time evolution of the dependence of the zonal and meridional component of the MWD on the cutoff length at the

altitude of 20 km for the three subdomains. Blue colours indicate that the drag decreases with cutoff, whereas red colours mean that it increases. Immediately we see that the desired band, where the MWD sensitivity to the cutoff length is near zero (indicated by white colour in the plots) is very narrow during some events and its location varies sharply over time.

For the zonal MWD component, the constant cutoff of 500 km indeed falls into the low sensitivity region for the SA and AP subdomains producing unbiased MWD estimates during some periods of the simulation. However, at other instants the white band is very narrow and fluctuating over a large range of wavelengths (from around 400 km to more than 1000 km).

As for the SG subdomain, the sensitivity here is generally stronger (in relative terms) than for AP and SA and the white band is even more variable over time, which might be related to the fact that the SG subdomain is the smallest one, as discussed in Section 5. Note that for SG in the first days of the analyzed period the sensitivity of the zonal MWD component shows red regions embedded between blue regions around the 800 km cutoff, meaning that the drag is increasing when allowing for both longer and shorter wavelengths besides the red region.

For the meridional MWD component, the estimates show sensitivity similar to the sensitivity of the zonal component. Only for the AP domain, the sensitivity is relatively weak and the constant cutoff of 500 km is an almost ideal choice except for some intermittent events. However, these findings hold only for the studied period and can change especially with a different background wind field and its orientation with respect to the topography.

The sensitivity of MWD estimates to the cutoff is further dependent on the altitude in question. In the Supplementary Material, we show the sensitivity of MWD components at 40 km. Generally speaking, for the upper stratospheric altitudes the sensitivity is smaller (presumably due to the dominant importance of vertically propagating GWs, as will be discussed further in the text). At tropospheric levels, the sensitivity is far stronger, but the hypothesis of the existence of the GW dominated part of the specific horizontal kinetic energy spectrum is increasingly invalid.

Altogether, the results suggest that the MWD estimates from the high-pass filter method may contain significant uncertainty due to the sensitivity on the cutoff value and it is generally not possible to choose a constant value of the parameter. For this reason, we propose two modifications to the method that sets the cutoff value in every time step using the information from the energy spectrum analysis.

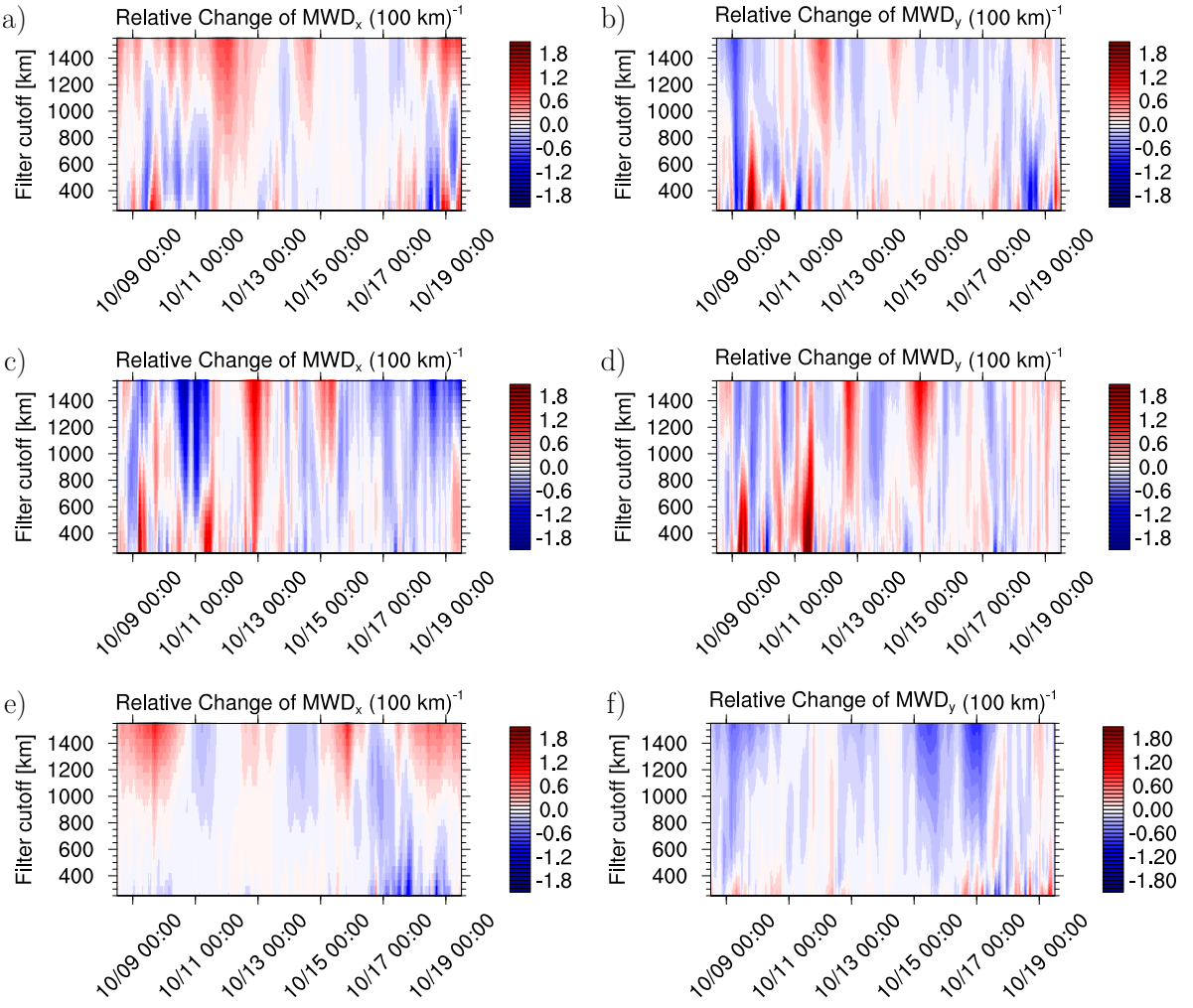

FIG. 5. Derivative of MWD components with respect to the cutoff for different subdomains: a) MWD_x, SA, b) MWD_y, SA, c) MWD_x, SG, d) MWD_y, SG, e) MWD_x, AP, f) MWD_y, AP. The colours code the relative MWD change with respect to the median of the absolute value of MWD computed over time and cutoff length. The two colours close to white represent the change of the MWD component smaller than 10 % of the median if the cutoff length is increased by 100 km.

c. Comparison of the Methods

The analysis of the total specific horizontal kinetic energy spectrum (averaged over 15 hours to eliminate local noise effects emerging from incomplete wave periods) provided two important natural bounds on the simulated GW spectrum. The first bound is the effective resolution, which is a limiting wavelength for the fully resolved waves by the model (the black bottom line in Fig. 3;

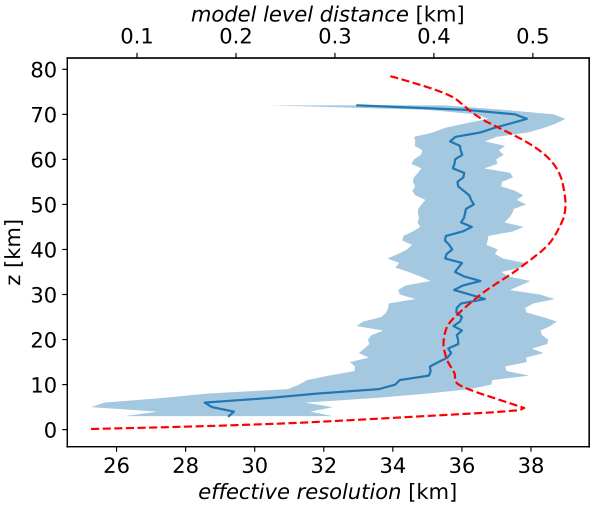

FIG. 6. Average vertical profile of effective resolution (blue line) with its variation (blue area) throughout the simulation. The red line depicts the average distance between two neighbouring vertical model levels.

Klaver et al. 2020). This bound is estimated as the wavelength at which the values in the horizontal spectrum of specific horizontal kinetic energy deviate significantly from a straight line fitted to the mesoscale part of the spectrum.

Fig. 6 shows that the vertical profile of effective resolution follows the variations of vertical resolution with height suggesting that vertical resolution of the model can be an important factor in our simulation, controlling the effective horizontal resolution. The connection of vertical resolution and the horizontal scale of resolved processes was studied e.g. in Skamarock et al. (2019a).

The effective resolution is evaluated from the spectrum for the entire domain and it does not necessarily mean that there are no waves with horizontal wavelengths shorter than this threshold. Locally, GW modes can be present with horizontal wavelengths smaller than the effective resolution that are resolved by the model due to the sufficiently long vertical wavelengths. By applying a low-pass filter to cut the shorter modes off, we would lose a part of the GW related information. Hence, for means of the GW separation the removal of the wavelengths shorter than the effective resolution is not beneficial. This is confirmed by visual comparison of the filtered fields with and without the application of a low-pass filter (Fig. 7).

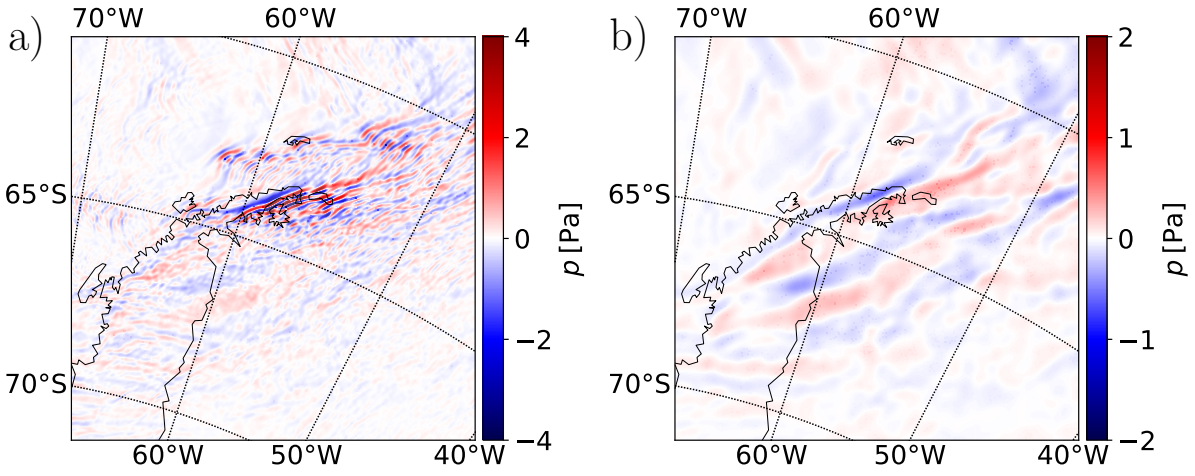

FIG. 7. Comparison of high-pass filter and a combination of high-pass and low pass filter. a) Perturbation field of the pressure obtained by high-pass filter method with the cutoff length computed from the slopes in the horizontal kinetic energy spectrum. b) Perturbation field of the pressure obtained by combination of high-pass filter and low-pass filter with the cutoff length for the low-pass filter set on the basis of the effective resolution.

The second bound, which can be derived from the total kinetic energy spectrum is the longest wavelength, until which the spectrum of horizontal kinetic energy follows the theoretical shape for the mesoscale spectrum (presumably GW dominated; upper black line in Fig. 3) introduced in the spectral slope method presented in Section 2c. An alternative natural bound is the intersection of divergent and rotational part from the spectrum decomposition introduced in the second part of Section 2c. We argue that choosing a cutoff based on the spectral information is a physically optimal approach, although it turns out that determination of this bound brings along a considerable level of uncertainty in both the spectral slope method and the divergence dominated method.

The reason why determining the upper bound on the GW part of the spectrum from the slopes is complicated can be seen e.g. for the altitude of 20 km in Fig. 8 (or for the altitude of 40 km in Fig. S6 in the Supplementary Material). The problem is that the horizontal kinetic energy spectra are not smooth in the range of wavelengths for which the bound is sought, but, near the upper bound, are dominated by individual modes. Therefore, an application of a simple algorithm based on fitting a line to a part of the GW dominated spectrum, which would terminate on the first random departure, could result in too small cutoff values. As we cannot a priori rule out the possibility that the dominant modes in this uncertain region are connected to GWs (e.g. inertia-

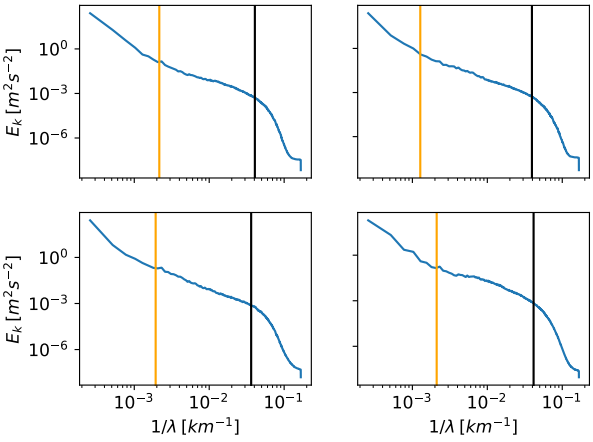

FIG. 8. GW range and effective resolution at 20 km. Example of spectra from nine randomly chosen time instants. The black vertical line denotes the effective resolution, the orange vertical line denotes the upper bound of the horizontal wavelengths with dominant GW.

GWs sourced by the orography in the domain; see Section 5), we have to apply a more advanced greedy algorithm, as described in Section 2d.

The mean vertical profiles and variability of the dynamically estimated cutoff for the analysed simulation using both methods are shown in Fig. 9. As for the spectral slope method (Fig. 9a), the mean cutoff is largest approximately between 20 km and 40 km, where it exceeds 1000 km. The cutoff gets gradually smaller both above in the upper stratosphere and mesosphere and below in the lower stratosphere. The mean cutoff is smaller than 500 km only above 60 km and below 10 km. This is reflecting the mean zonal wind profile (see Fig. 14 in Kruse et al. (2022)) with a tentative explanation that the maximal wavelength of vertically propagating GWs is decreasing with the decreasing background winds in the upper stratosphere. Numerical damping as cause for this effect can be excluded in this WRF configuration. In this lower to middle tropospheric region, it is generally not expected that GWs will dominate any part of the horizontal kinetic energy spectrum and we do not produce MWD estimates in this region. The time variability of the cutoff value at all levels in the stratosphere is large and the standard deviation is of a similar magnitude as the mean cutoff.

The vertical profile of the cutoff value obtained by the divergence dominated method is shown in Fig. 9b. Similarly to the spectral slope method, the cutoff values are continuously rising from the troposphere. Above the altitude of approximately 15 km, the mean cutoff value remains about

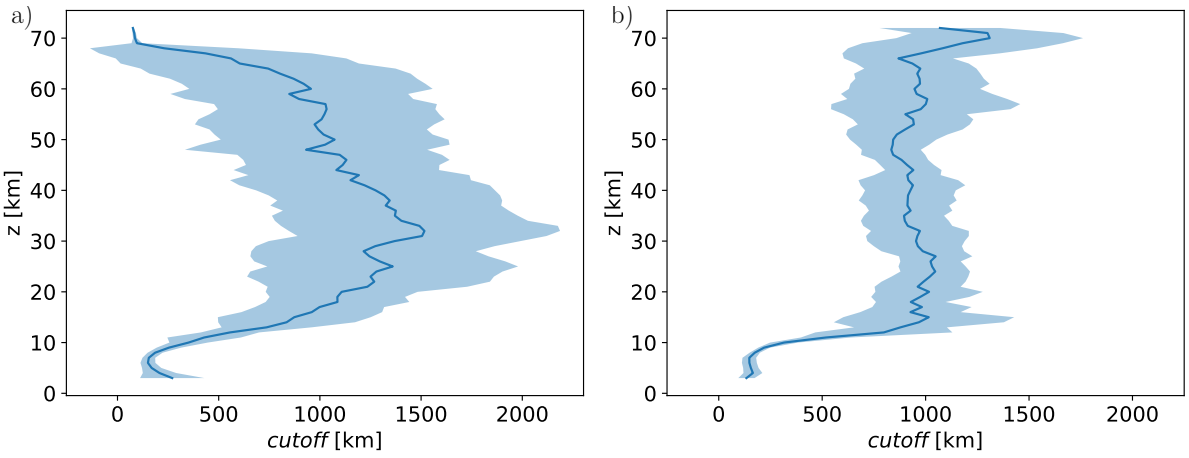

FIG. 9. Mean vertical profile of the cutoff parameter. The filled region depicts the standard deviation corresponding to the temporal variability. a) Spectral slopes method. b) Divergence dominated method.

approximately 1000 km, with less pronounced altitude variability than in the spectral slope method. On the other hand, the shaded area in the plot still show high temporal variability. Within the range given by the standard deviation, the cutoff values obtained by this method vary mostly between 750 and 1250 km. The agreement between the two methods further supports the choice of a GW separation method with a time varying cutoff.

A significant difference between the cutoff profiles in Fig. 9 is the decrease of cutoff above the altitude of 60 – 65 km for the spectral slope method, that is not present in the plot for divergence dominated method. The reason is that the shape of the kinetic energy spectra at these altitudes changes so that there is no clear separation into parts with different slopes and the spectral slope method is therefore unreliable at the higher levels.

Next, MWD estimates from the dynamical cutoff methods are compared with the original high-pass filter method for a constant value of the cutoff length 500 km, which is used in Kruse et al. (2022), and also with the S3D method. In Fig. 10, the zonal and meridional MWD estimates from the two methods with variable cutoff and a method with a constant cutoff are compared at 20 km for each hotspot (Fig. S7 in the Supplementary Material depicts the estimates at 40 km). As suggested by the sensitivity analysis in Fig. 5 and the large variability of the dynamical cutoff estimates in time, the difference between the methods depends on time and also on the hotspot region (and altitude). For AP, the episodes of larger differences between the MWD estimates are

rather sporadic. For SA and SG the differences have larger magnitude and are more frequent. For the meridional MWD component the differences are smaller.

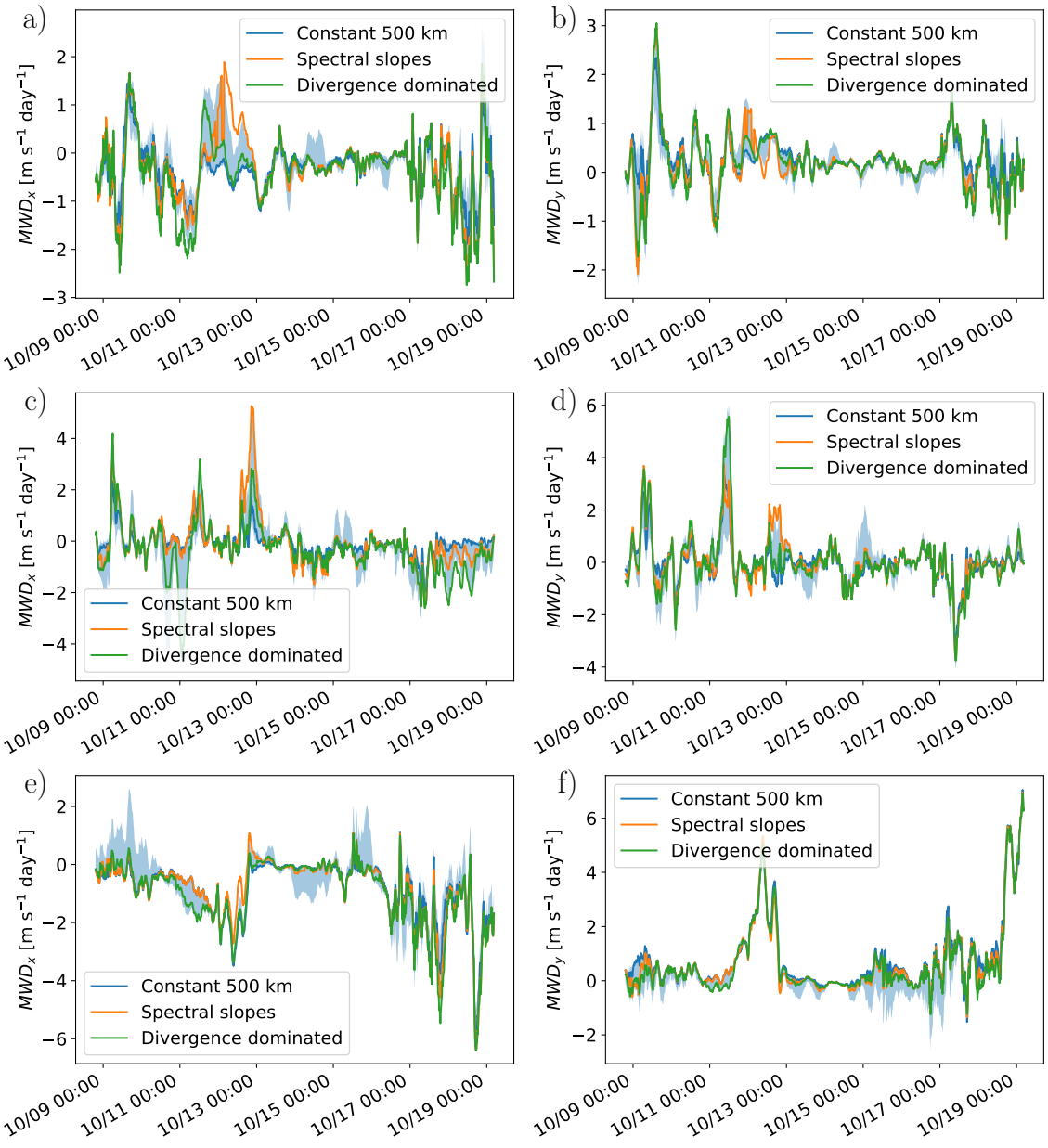

459 FIG. 10. Comparison of the improved method and high-pass filter method with constant cutoff at 20 km:
460 a) MWD_x, SA, b) MWD_y, SA, c) MWD_x, SG, d) MWD_y, SG, e) MWD_x, AP, f) MWD_y, AP. The orange and
461 green lines visualize the time evolution of MWD computed using the wave perturbation from the methods with
462 dynamically changing cutoff. The blue lines describe the evolution of MWD using the high-pass filter method
463 with constant cutoff length 500 km. The filled blue regions represent the possible values of MWD in individual
464 times for the cutoff range 250 – 1550 km.

Regarding the S3D method, vertical momentum fluxes that are derived from the S3D temperature perturbation are well correlated with the momentum fluxes obtained from perturbations separated by the methods with Gaussian filter, even though the values are lower. This is easily understandable as the wavelengths from the S3D method in our configuration cannot be larger than 500 km and the contribution from long waves is therefore missing. However, the S3D method encounters difficulties when evaluating the resulting drag, because the method is not continuous (different sines can be fitted in adjacent levels) and therefore the vertical derivative of momentum fluxes creates noise at some timesteps. Up to these noise perturbations, the time evolution of the vertical drag from the S3D method is similar to the other methods (not shown), but its magnitude is generally significantly lower.

Statistical differences between the four methods at the altitude of 20 km are summarised in Table 1. Given the fact that the results derived from the S3D method contain a few nonphysical outliers and that the distributions of MWD are slightly distinct from the normal distribution (especially in the fact that they are showing much longer tails), we used the median and interquartile range (IQR) instead of the mean and the variance for the comparison in order to obtain a more robust statistical description.

The median values of the derivatives of the flux of the zonal momentum (MWD_{xx}, MWD_{yx}, MWD_{zx}) range from -0.39 to 0.00 for the high-pass filter methodologies and from -0.08 to 0.06 for the S3D method, with the IQR larger than the median, signifying high variability and intermittency seen already in Fig. 10. Comparing the individual methods, we can generally see that the median and IQR differences between the methods are smaller between the dynamical cutoff methods than between each of them and the constant cut-off method. The pronounced differences between IQRs of MWD_{xx}, MWD_{yx} and MWD_{zx} (being generally smaller for the method with constant cutoff than for the spectral based method) mean that for individual events the difference of actual drag estimates can be more than 100 % larger than the median difference suggests.

Similar statistics are shown in Table 2 for the altitude of 40 km. Here the median MWD estimates for all methods and regions are larger and hence the IQR is smaller than at 20 km in relative terms. The difference in median MWD values between the methods is around 10 % of the MWD median value and similarly for the IQR estimates. The drag estimated by the constant cutoff methodology

		MWD_x		MWD_{xx}		MWD_{yx}		MWD_{zx}	
		Median	IQR	Median	IQR	Median	IQR	Median	IQR
Constant cutoff	SA	-0.26	0.49	-0.01	0.07	-0.01	0.06	-0.23	0.50
	AP	-0.47	1.16	-0.03	0.07	-0.04	0.10	-0.39	1.00
	SG	-0.09	0.40	-0.01	0.13	0.00	0.10	-0.09	0.43
Spectral slopes	SA	-0.22	0.63	0.00	0.17	0.00	0.14	-0.24	0.60
	AP	-0.47	1.13	-0.05	0.15	-0.07	0.18	-0.36	0.95
	SG	-0.20	0.69	-0.09	0.30	0.00	0.38	-0.12	0.71
Divergence dominated	SA	-0.27	0.60	0.00	0.17	-0.01	0.12	-0.28	0.61
	AP	-0.58	1.49	-0.09	0.21	-0.03	0.12	-0.37	1.08
	SG	-0.31	0.87	-0.16	0.35	-0.02	0.52	-0.15	0.80
S3D	SA	-	-	-	-	-	-	-0.06	0.74
	AP	-	-	-	-	-	-	-0.08	0.35
	SG	-	-	-	-	-	-	0.06	0.36

TABLE 1. Medians and interquartile ranges (IQR) for zonal MWD and its components using different methods at the altitude 20 km. Values are given in m $s^{-1}day^{-1}$.

is generally smaller than for the two variable cutoff methods for all regions and components, but its vertical component is still much stronger than from the S3D method.

A notable aspect of the results for both altitudes is that the differences between high-pass filter methods in median MWD_{xx} and MWD_{yx} estimates are of comparable magnitude with the differences in MWD_{zx} despite the median MWD_{zx} drag being stronger by an order of magnitude. This means that the relative uncertainty in these MWD_{xx} and MWD_{yx} terms connected with horizontal flux divergences is much bigger.

To sum up, there are large differences between MWD estimates from S3D and high-pass filter methods and although the assumption of a constant cutoff does not result in pronounced systematic biases of the zonal MWD or its components, the estimates from the dynamic methods can lead at individual events to differences larger than the order of magnitude of the median MWD values.

When we focus on individual events at 20 km, one of the most pronounced differences between the methods can be seen on 12^{th} October for the zonal MWD component in SA (Fig. 10a). The MWD_x estimate from the constant cutoff method was small but negative, whereas the spectral slope method (and with small time-shift also the divergent dominated method) estimated strong acceleration up to 2 m $s^{-1}day^{-1}$. This event is reflected also in differences of the meridional MWD in SA (Fig. 10b), even though the magnitude of the difference is not as pronounced as for the zonal component.

		MWD_x		MWD_{xx}		MWD_{yx}		MWD_{zx}	
		Median	IQR	Median	IQR	Median	IQR	Median	IQR
Constant cutoff	SA	-15.8	20.8	-0.6	1.1	0.5	1.4	-15.5	23.5
	AP	-11.6	22.1	-1.0	2.0	-0.3	0.8	-10.2	19.5
	SG	-5.3	12.3	-0.4	2.7	0.4	1.4	-5.8	11.1
Spectral slopes	SA	-16.2	20.5	-0.9	1.9	0.4	1.3	-15.6	21.2
	AP	-13.0	23.2	-1.3	3.1	-0.3	1.0	-9.7	18.9
	SG	-6.2	13.8	-0.7	4.6	0.4	2.0	-6.3	11.7
Divergence dominated	SA	-16.4	20.6	-0.9	1.9	0.7	1.6	-15.9	24.3
	AP	-12.9	23.8	-1.5	3.0	-0.4	1.4	-10.2	20.5
	SG	-6.3	13.8	-0.7	4.8	0.6	2.5	-6.4	12.0
S3D	SA	-	-	-	-	-	-	-12.9	23.8
	AP	-	-	-	-	-	-	-8.4	13.9
	SG	-	-	-	-	-	-	-3.4	17.7

TABLE 2. Medians and interquartile ranges (IQR) for zonal MWD and its components using different methods at the altitude 40 km. Values are given in m $s^{-1}day^{-1}$.

For the SG subdomain (Figures 10c and 10d), a similar pronounced difference occurs slightly later, around 12th October, 20:00. A tentative hypothesis mentioned already in the previous section, is the horizontal propagation of waves with wavelengths larger than the wavelengths corresponding to the chosen constant cutoff value (probably downstream propagating inertia-GWs), which would not be captured by the method with constant cutoff in both subdomains. The fact that in the divergence dominated method the values are also not so high in this time period supports this hypothesis, as this method might also be able to capture inertia-GWs only to some extent because of their contribution to the rotational component. For the AP subdomain around 12th October, there are also visible differences between the estimates of both MWD_x and MWD_y, although smaller than for the other two subdomains due to the smaller sensitivity of the MWD around this date in AP.

d. Impact of GWs with Larger Horizontal Wavelengths

In this subsection, we study the sensitivity of individual parts contributing to the zonal MWD component, i.e. the zonal divergence of a zonal flux of zonal momentum (MWD_{xx}), meridional divergence of a meridional flux of zonal momentum (MWD_{yx}) and vertical divergence of a vertical flux of zonal momentum (MWD_{zx}).

The sensitivity of those contributions for each hotspot is shown in Fig. 11. Generally, for all subdomains, the dependence is much stronger for the parts with horizontal divergence MWD_{xx} and

MWD_{yx} than for MWD_{zx}. Because the sensitivity expresses the fact that the choice of the cutoff length determines the accepted portion of GW modes, this means that the horizontal flux components are more exclusively connected with GW modes with longer horizontal wavelengths than the vertical flux components, as expected from linear theory and observed by aircraft (Smith and Kruse 2017) - the horizontal wave momentum flux components compared to the vertical fluxes are more exclusively connected with GW modes with longer horizontal wavelengths that are increasingly affected by rotation (Teixeira 2014). Another important aspect is that the sensitivity of the horizontal flux contributions has often an opposite sign, which means that the large sensitivities of those two components partially compensate and do not fully project to the net MWD_x.

The sensitivities are reflected in differences of MWD_{xx}+ MWD_{yx} and MWD_{zx} estimates between the constant and dynamically determined cutoff methodologies (Fig. 12 for the altitude of 20 km). For the component MWD_{zx}, all the compared methods produce very similar estimates, except for the period around 11$^{\text{th}}$ and 12$^{\text{th}}$ October, when the determined cutoff is exceptionally large (up to 2000 km for spectral slope mathod and 1500 km for divergence dominated method). The differences in the horizontal components are more pronounced during the whole simulation. Both the methods with the dynamically set cutoff generally lead to substantially higher magnitudes of the components MWD_{xx} and MWD_{yx}. For all hotspots, we can find large differences on 12$^{\text{th}}$ October, but for each hotspot individually there are more events with pronounced differences. For example, for SA and AP we can see for the horizontal components large differences between the spectral slope method and the constant cutoff method between 17$^{\text{th}}$ and 19$^{\text{th}}$ October, but with only small differences in MWD_{zx}. The fact that the sensitivity is, for some events, higher for the horizontal components even in the absolute numbers, is noticeable from the shaded regions in Fig 12.

The different sensitivity to the methodology of the derivatives of the zonal momentum flux MWD_{xx}, MWD_{yx} and the MWD_{zx} is confirmed and quantified by the correlations between the time series of the MWD_x component estimates using the methods with dynamically changing cutoff and the method with constant cutoff. The Pearson correlation coefficient is for MWD_{zx} for all subdomains and tested altitudes close to one (third column in Tab. 3), whereas for the components MWD_{xx} and MWD_{yx}, the values are significantly lower (first two columns in Tab. 3).

		MWD_{xx}	MWD_{yx}	MWD_{zx}
Spectral slopes	SA	0.76	0.21	0.88
	AP	0.73	0.29	0.96
	SG	0.52	0.68	0.91
Divergence dominated	SA	0.69	0.51	0.90
	AP	0.64	0.59	0.97
	SG	0.36	0.51	0.81

TABLE 3. Pearson correlation coefficient between the methods with constant and dynamically changing cutoff for the components of zonal drag MWD_x the altitude 20 km.

Regarding the sensitivity and differences between components of the meridional drag MWD_y, the results are almost identical as for the zonal MWD components with sensitivity of the horizontal divergence parts being stronger and leading to larger differences in corresponding meridional MWD components (Figs. S10 and S12 in the Supplementary Material) Also, similar results can be derived for the level of 40 km (Figs. S8 and S9 for the zonal component and Figs. S11 and S13 for the meridional component).

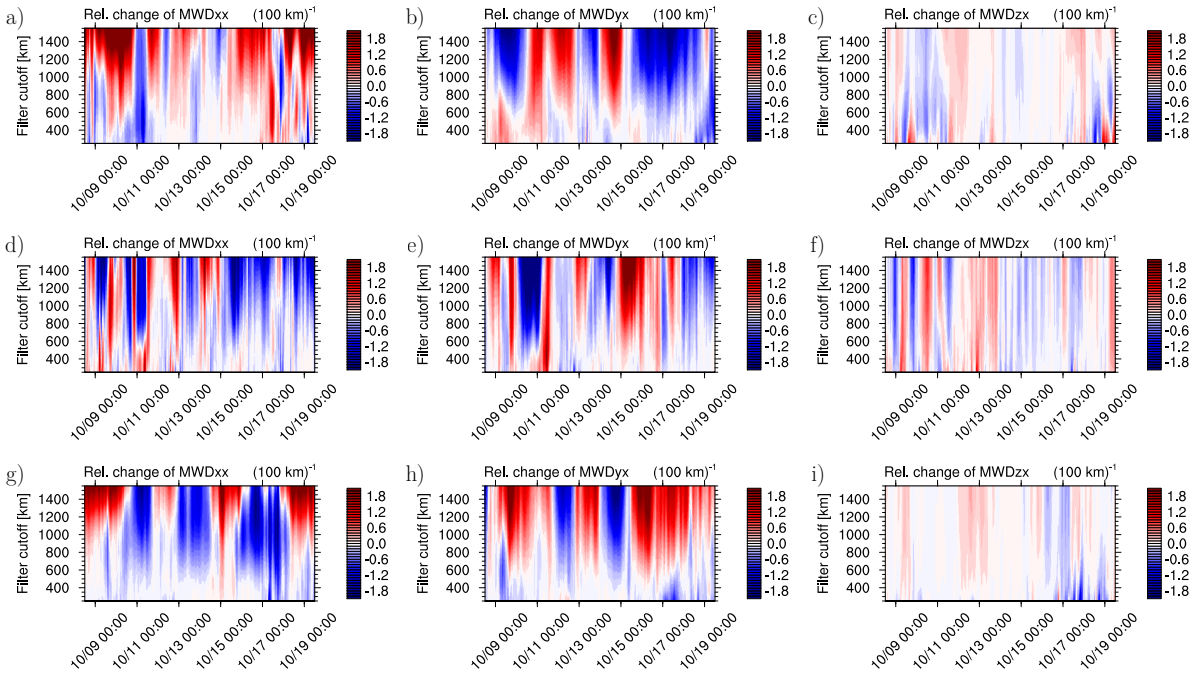

570 FIG. 11. Derivative of MWD_x components with respect to the cutoff, rescaled by the median, at the altitude
571 of 20 km for different subdomains: a) MWD_{xx}, SA, b) MWD_{yx}, SA, c) MWD_{zx}, SA, d) MWD_{xx}, SG, e) MWD_{yx},
572 SG, f) MWD_{zx}, SG, g) MWD_{xx}, AP, h) MWD_{yx}, AP, i) MWD_{zx}, AP. The colours code the relative change
573 of the derivative of the horizontal momentum flux (MWD_{xx}, MWD_{yx}, MWD_{zx}) with respect to the median of the
574 absolute value of the quantities computed over time and cutoff length. The two colours close to white represent
575 the change of the quantities smaller than 10 % of the median if the cutoff length is increased by 100 km.

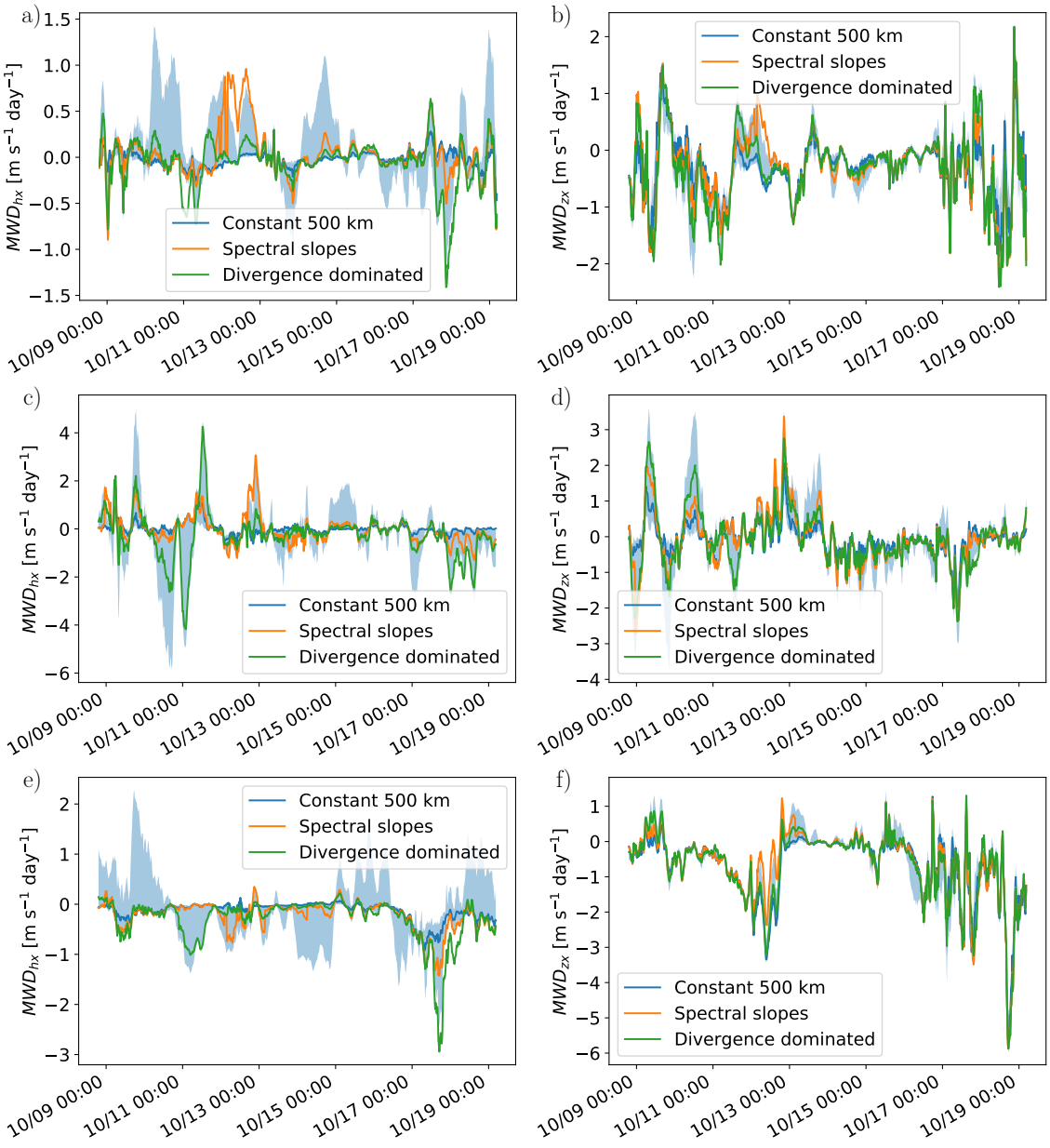

576 FIG. 12. Comparison of the improved method and high-pass filter method with constant cutoff at 20 km for hor-
577 izontal and vertical part of MWD_x and different subdomains: a) MWD_{hx}=MWD_{xx}+MWD_{yx}, SA, b) MWD_{zx},
578 SA, c) MWD_{hx}, SG, d) MWD_{zx}, e) MWD_{hx}, AP, f) MWD_{zx}, AP. The orange and green lines visualize the time
579 evolution of MWD_{hx} or MWD_{zx} computed using the wave perturbation from the methods with dynamically
580 changing cutoff. The blue lines describe the evolution of MWD_{hx} or MWD_{zx} using the high-pass filter method
581 with constant cutoff length 500 km. The filled blue regions represent the possible values of MWD_{hx} or MWD_{zx}
582 in individual times for the cutoff range 250 – 1550 km.

5. Discussion and Conclusions

Due to their simplicity, high-pass filtering methods based on Fourier (Kruse and Smith 2015; Gisinger et al. 2017) or cosine (Van Niekerk et al. 2018b) transforms are widely used in atmospheric physics to identify GW perturbations in high-resolution simulation data. The uncertainty of the GWD estimates connected with the a priori choice of the cutoff parameter used in the methods has nevertheless not been studied to date. In the present study, we address this problem to show that it is not possible to choose a universal constant cutoff parameter.

When studying the dependence of the zonal and meridional drag component MWD_x and MWD_y estimates on the cutoff length, the results are notably sensitive to the choice of the cutoff for the whole range of admissible cutoffs. However, when considering individual parts of the drag, the studied quantities can be divided into two groups - those including vertical velocity (i.e. vertical fluxes), and purely horizontal terms. The sensitivity of terms involving vertical velocity is generally lower than the sensitivity of terms without it. In Kruse and Smith (2015), such kind of behaviour is hypothesized to be caused by the shape of the vertical velocity spectrum. Also, these results support the hypothesis that the sensitivity of the high-pass filter method is caused mainly by the horizontally propagating GWs with large horizontal wavelengths, which contribute strongly to the horizontal derivatives of the horizontal fluxes of the horizontal momentum, modifying the net value of the drag.

The sensitivity of the method on the cutoff length motivates modifying methods for a variable cutoff parameter. The horizontal energy spectra were analysed to estimate the optimal cutoff value. In general, the spectral analysis indicates that for the studied region and time the traditionally used cutoff is too small. The cutoff is dependent also on the altitude, hence we estimate it at each time step and altitude separately. This modification causes a moderate slowdown of the methods but on the other hand, it arguably reduces the uncertainty of the traditional high-pass filter method drag estimates. Our comparisons show that in some cases the difference between MWD estimates of the constant and dynamically set-up cutoff methods can be of the same order of magnitude as the estimates.

Compared to Kruse et al. (2022), inertia-GWs (Dunkerton 1984) and even internal Rossby-GWs (Teixeira and Grisogono 2008) sourced by the orography in the domain may be increasingly sampled as we allow for larger cut-off values. The inclusion of the longer modes to the analysis of dedicated

high-resolution simulations is beneficial, especially if one is concerned about the horizontal fluxes of horizontal momentum and the resulting drag components. Particularly, inertia-GWs have been shown to play a role in model sensitivity to vertical resolution, as vertical resolutions of around 100m would be needed to fully resolve them, even though the horizontal resolution may be sufficient (Skamarock et al. 2019a). For the general circulation models, the sensitivity of the resolved GW momentum flux on vertical resolution in the stratosphere and mesosphere has been demonstrated before by Watanabe et al. (2015). Recently, equatorial-trapped inertia-GWs with fine vertical scales have been identified by observations with unprecedented vertical resolution in the tropical UTLS (Bramberger et al. 2022), with yet unquantified importance for stratospheric dynamics, QBO and cirrus cloud formation.

However, also these waves with larger horizontal wavelength are not fully represented in the current generation numerical weather prediction and climate models due to the coarse vertical resolution (Skamarock et al. 2019a) and hence we incorporate them to our MWD estimates.

There are several aspects that contaminate the accuracy of the modified methods as well. The most pressing drawback of the methods with dynamic cutoff is the uncertainty emerging during the cutoff specification. As already mentioned, the part of the horizontal kinetic energy spectrum between GWs and synoptic scale motions is dominated by individual modes that cannot be easily attributed as GWs/nonGWs but might be rather connected to e.g. inertia-GWs or Rossby-GWs. Also, the determination of the wavelength where the slope of the spectrum changes or the wavelength of the intersection of divergent and rotational components is performed in a logarithmic plot. Hence, the effect of a small error of specification in the spectrum can result in relative large error in the cutoff length. This has negative impact on the accuracy of the MWD estimates. However, note that for acceptable detection algorithms the error from using a constant cutoff shall be always higher.

Another issue is that the proposed modified methods use larger cutoff lengths. Therefore, one should pay attention to the choice of subdomains at which the quantities are evaluated. First, the subdomain size should be large enough, so that the present waves can be averaged over the subdomain. Otherwise, the assumptions of the technique applied for evaluation of MWDs and MFs might not be satisfied and the results might be affected by the presence of wave perturbations whose average over the subdomain is not zero. This can be the case for the smallest hotspot,

SG, during events with large cutoffs. Nevertheless, the comparison of the modified and constant cutoff high-pass filter methods did not produce qualitatively different results between SG and other hotspots, which are large enough not to be affected. Second, in the applied filtering procedures, the use of a larger cutoff implies that artificial perturbations penetrate farther away from the domain boundaries (for a detailed discussion, see Kruse and Smith (2015)). The subdomains thus need to be distant enough from the outer boundary. Otherwise, the use of the cosine transform instead of the Fourier transform or the application of another periodization method that does not generate small-scale oscillation is advisable.

Although we analyzed only a regional simulation with a limited time-span, it is reasonable to expect that the cutoff sensitivity of the GW momentum flux and drag estimates is a robust feature, which will be pronounced particularly in the presence of horizontally propagating GWs. Even though this effect might cancel out climatologically, in short-term studies, this can cause large uncertainties of the GW momentum flux and drag estimates.

The proposed methodologies are aimed at dedicated analyses of GWs and their interactions in high-resolution model simulations on regional domains. But as such they can also help to provide constraints for the GW parameterization schemes in global models. Particularly, with the shift towards scale-aware GW parameterizations (e.g. van Niekerk and Vosper, 2021) it becomes important to have a good knowledge of the parameterized source contribution over a spectral range as wide as possible and as accurate as possible. Given the spatial and temporal variability of the affected scales, variable cut-off is essential to quantify the effects of the parameterized source.

Further improvement of the methods (especially regarding the precision of the cutoff specification) is the object of further research. Alternatively, the filtering can be performed by Lagrangian approaches in the internal frequency domain, as demonstrated by Shakespeare et al. (2021) for GWs in the ocean. Also, we plan to compare the MWD estimates with other methodologies that have not been used to estimate resolved GWD from simulations to date. Nevertheless, we argue that the dynamic cutoff methods proposed here based on the underlying spectral analysis presents a step forward in providing more accurate estimates of MWD from high-resolution model simulations.

Acknowledgments. The authors would like to acknowledge discussions with Inna Politchouk, Annelize van Niekerk and Ryosuke Shibuya within the New Quantitative Constraints on Orographic Gravity Wave Stress and Drag Satisfying Emerging Needs in Seasonal-to-Subseasonal and Climate Prediction international team at the ISSI Bern, which helped to shape and conceptualise the paper. Also, Zuzana Procházková and Petr Šácha want to acknowledge discussions with Aurélien Podglajen. Manfred Ern was supported by the German Research Foundation (DFG) grant ER 474/4-2 and by the German Federal Ministry of Education and Research (BMBF) grant 01LG1905C (QUBICC, ROMIC). Sonja Gisinger was supported by the German Federal Ministry for Education and Research (01LG1907, WASCLIM, ROMIC program). Corwin Wright acknowledges Royal Society University Research Fellowship URF21023. Zuzana Procházková was supported by GAČR 21-20293J and GAUK 281021 and Petr Šácha and Zuzana Procházková further acnowledge the funding from the Czech Science Foundation under the Junior Star grant 23-04921M.

Data availability statement. For the study, WRF model output data from Kruse et al. (2022) was used. As the size of this data is approximately 14 TB, we cannot guarantee long-term availability. Preprocessed data used for the generation of the plots and the analysis codes can be made available on request.

APPENDIX A

Specific Horizontal Kinetic Energy Computation

Horizontal kinetic energy at an altitude z with a unitary density is given by

$$\begin{aligned} E^z =& \frac{1}{2} \int \int \left(u^2(x,y,z) + v^2(x,y,z) \right) \mathrm{d}x \, \mathrm{d}y \\ \approx& \frac{1}{2} \sum_{i=0}^{N-1} \sum_{j=0}^{N-1} \left(u_{i,j}^2 + v_{i,j}^2 \right) (\Delta x)^2, \end{aligned} \tag{A1}$$

where $u_{i,j} = u(x_i, y_j)$ and $v_{i,j} = v(x_i, y_j)$ are the horizontal velocity components at individual grid points, N denotes number of grid point in each direction and Δx is the horizontal distance between grid points for both x and y directions.

To evaluate the spectrum, it is convenient to describe the energy in the Fourier space. We use the definition of the two-dimensional discrete Fourier transform (DFT)

$$\hat{a}_{k,l} = \sum_{n=0}^{N-1}\sum_{m=0}^{N-1} a_{n,m} \mathrm{e}^{-2\pi \mathrm{i}\frac{nk}{N}} \mathrm{e}^{-2\pi \mathrm{i}\frac{ml}{N}}, \quad k,l = 0,\ldots,N-1, \tag{A2}$$

with its inverse

$$a_{m,n} = \frac{1}{N^2}\sum_{k=0}^{N-1}\sum_{l=0}^{N-1} \hat{a}_{k,l} \mathrm{e}^{2\pi \mathrm{i}\frac{nk}{N}} \mathrm{e}^{2\pi \mathrm{i}\frac{ml}{N}}, \quad m,n = 0,\ldots,N-1. \tag{A3}$$

By the Parseval theorem for two-dimensional DFT given by equation (A2) (Sundararajan 2001), it holds

$$\sum_{i=0}^{N-1}\sum_{j=0}^{N-1}\left(u_{i,j}^2 + v_{i,j}^2\right) = \frac{1}{N^2}\sum_{k=0}^{N-1}\sum_{l=0}^{N-1}\left(\hat{u}_{k,l}\hat{u}_{k,l}^* + \hat{v}_{k,l}\hat{v}_{k,l}^*\right) \tag{A4}$$

with $\hat{u}_{k,l}$ and $\hat{v}_{k,l}$ obtained by the DFT of the velocity components. The symbol $*$ denotes the complex conjugate. The latter expression can already be used to compute specific horizontal kinetic energy for individual wave numbers $k,l = 0,\ldots,N-1$ as

$$E_{k,l}^z = \frac{1}{2N^2}\left(\hat{u}_{k,l}\hat{u}_{k,l}^* + \hat{v}_{k,l}\hat{v}_{k,l}^*\right). \tag{A5}$$

This equality can be also rewritten to use the horizontal Fourier transform of the horizontal divergence δ and the horizontal vorticity ζ. As these quantities are defined as a sum of derivatives of velocity components, their Fourier transform can be evaluated from algebraic expressions

$$\hat{\zeta}_{k,l}^z = \frac{2\pi\mathrm{i}}{N\Delta x}\left(k\hat{v}_{k,l} - l\hat{u}_{k,l}\right), \tag{A6}$$

$$\hat{\delta}_{k,l}^z = \frac{2\pi\mathrm{i}}{N\Delta x}\left(k\hat{u}_{k,l} + l\hat{v}_{k,l}\right). \tag{A7}$$

These equations imply that

$$\hat{\zeta}_{k,l}^z(\hat{\zeta}_{k,l}^z)^* + \hat{\delta}_{k,l}^z(\hat{\delta}_{k,l}^z)^* = \left(\frac{2\pi}{N\Delta x}\right)^2\left(k^2+l^2\right)\left(\hat{u}_{k,l}\hat{u}_{k,l}^* + \hat{v}_{k,l}\hat{v}_{k,l}^*\right), \tag{A8}$$

which means, that Eq. (A5) can be replaced by equation

$$E^z_{k,l} = \frac{1}{2N^2} \frac{\hat{\zeta}^z_{k,l}(\hat{\zeta}^z_{k,l})^* + \hat{\delta}^z_{k,l}(\hat{\delta}^z_{k,l})^*}{\left(\frac{2\pi}{N\Delta x}\right)^2 \left(k^2 + l^2\right)} \tag{A9}$$

for $k, l = 0, \ldots, N-1$, that can be simply decomposed into divergent and rotational part.

To obtain a 1D spectrum (either from Eq. (A5), or for the divergent and rotational part from Eq. (A9)), we denote

$$K^2 \equiv \left(\frac{2\pi}{N\Delta x}\right)^2 \left(k^2 + l^2\right) \tag{A10}$$

the square of the size of horizontal wave vector corresponding to the horizontal wavelength $\lambda = 2\pi/K$. As we need the spectrum with respect to the horizontal wavelength, we sum up the values $E^z_{k,l}$ of specific energy with similar values of K (Blažica et al. 2013; Sun et al. 2017). More precisely, we consider the sequence of horizontal wavenumbers

$$K_n = \frac{2\pi}{N\Delta x} n, \quad n = 1, 2, \ldots, \left[\frac{N}{2}\right] - 1 \tag{A11}$$

with the upper bound corresponding to the Nyquist frequency. We further denote

$$\Delta K = \frac{2\pi}{N\Delta x} \tag{A12}$$

the difference between two consecutive wavenumbers of this sequence. The specific horizontal kinetic energy spectrum is then computed by Eq.

$$E^z(K_n) = \sum_{|(k,l)|\Delta K \in I_n} E^z_{k,l}, \tag{A13}$$

where $I_n = (K_n - \Delta K/2, K_n + \Delta K/2)$ is an interval around K_n. The energy $E^z(K_n)$ is not the radial part of the 2D spectrum (in this case, the sum in the last equality would contain a factor K), but rather an average of the energy over wavenumbers near K_n.

APPENDIX B

Gravity Wave Drag in Cartesian Coordinates

We start by considering compressible inviscid flow on a rotating sphere. Using the standard scale-analysis argumentation (Cushman-Roisin and Beckers 2011), it is possible to write governing equation for the horizontal velocity components in the corotating coordinate system in the form

$$\partial_t u + u\partial_x u + v\partial_y u + w\partial_z u = -\frac{1}{\rho}\partial_x p + fv \tag{B1a}$$

$$\partial_t v + u\partial_x v + v\partial_y v + w\partial_z v = -\frac{1}{\rho}\partial_y p - fu, \tag{B1b}$$

where u, v and w are zonal, meridional and vertical wind components, p is the pressure and f is the Coriolis parameter.

We apply a linear perturbation method, assuming that the velocity components can be decomposed into a slowly varying mean flow and a small perturbation corresponding to the wave motion,

$$u = \langle u \rangle + u', \tag{B2a}$$

$$v = \langle v \rangle + v', \tag{B2b}$$

$$w = w', \tag{B2c}$$

where the mean vertical velocity component is taken zero. We further assume that the density is a function of altitude only. In computations, this is achieved by taking integral mean value of density $\hat{\rho}(z)$ over respective levels.

Next, we demonstrate the derivation for zonal momentum equation (B1a) only, the steps for the meridional component are analogous. With use of the continuity equation

$$\partial_t \rho + \partial_x(\rho u) + \partial_y(\rho v) + \partial_z(\rho w) = 0, \tag{B3}$$

it is possible to pass from (B1a) to the equation in the flux form

$$\partial_t(\rho u) + \partial_x(\rho u^2) + \partial_y(\rho uv) + \partial_z(\rho uw) = -\partial_x p + \rho f v. \tag{B4}$$

Substituting the decomposition (B2) and the assumption on density, we get

$$\begin{aligned}\partial_t\left(\langle u\rangle+u'\right)+\partial_x\left(\left(\langle u\rangle+u'\right)^2\right)+\partial_y\left(\left(\langle u\rangle+u'\right)\left(\langle v\rangle+v'\right)\right)\\ +\frac{1}{\hat{\rho}}\partial_z\left(\hat{\rho}\left(\langle u\rangle+u'\right)w'\right)\\ =-\frac{1}{\hat{\rho}}\partial_x p+f\left(\langle v\rangle+v'\right).\end{aligned} \tag{B5}$$

At this stage, we average (B5) over area A of the selected horizontal domain, which will be denoted by line over the quantities.

With the assumption that the perturbations of velocity components have zero average over the domain at every altitude and that the velocity field is such that the interchange of derivative and integral is possible, the first term is averaged to

$$\overline{\partial_t\left(\langle u\rangle+u'\right)}=\partial_t\overline{\langle u\rangle}. \tag{B6}$$

Using the fundamental theorem of calculus, the averages of the second and the third term in (B5) are

$$\overline{\partial_x\left(\left(\langle u\rangle+u'\right)^2\right)}=\frac{1}{A}\left[\int\left(\langle u\rangle+u'\right)^2\mathrm{d}y\right]_{x_1}^{x_2}, \tag{B7}$$

$$\overline{\partial_y\left(\left(\langle u\rangle+u'\right)\left(\langle v\rangle+v'\right)\right)}=\frac{1}{A}\left[\int\left(\langle u\rangle+u'\right)\left(\langle v\rangle+v'\right)\mathrm{d}x\right]_{y_1}^{y_2}. \tag{B8}$$

For the last integral on the left-hand side of (B5), we have

$$\frac{1}{\hat{\rho}}\overline{\partial_z\left(\hat{\rho}\left(\langle u\rangle+u'\right)w'\right)}=\frac{1}{A}\frac{1}{\hat{\rho}}\partial_z\iint\hat{\rho}\left(\langle u\rangle+u'\right)w'\,\mathrm{d}x\,\mathrm{d}y. \tag{B9}$$

If we further consider the average of $\langle\cdot\rangle\,(\cdot)'$ over faces to be zero, the previous three averaged terms can be thus simplified to

$$\overline{\partial_x\left(\left(\langle u\rangle+u'\right)^2\right)}=\frac{1}{A}\left[\int\left(\langle u\rangle^2+\left(u'\right)^2\right)\mathrm{d}y\right]_{x_1}^{x_2}, \tag{B10}$$

$$\overline{\partial_y\left(\left(\langle u\rangle+u'\right)\left(\langle v\rangle+v'\right)\right)}=\frac{1}{A}\left[\int\left(\langle u\rangle\langle v\rangle+u'v'\right)\mathrm{d}x\right]_{y_1}^{y_2}, \tag{B11}$$

$$\frac{1}{\hat{\rho}}\overline{\partial_z\left(\hat{\rho}\left(\langle u\rangle+u'\right)w'\right)}=\frac{1}{A}\frac{1}{\hat{\rho}}\partial_z\iint\hat{\rho}u'w'\,\mathrm{d}x\,\mathrm{d}y. \tag{B12}$$

To deal with the right-hand size of equation (B5), we write the velocity as a sum of velocities of geostrophic and ageostrophic flow, $u=u_g+u_a$, $v=v_g+v_a$. Geostrophic flow is an idealized stationary flow described by the balance of pressure and Coriolis force, considering advective terms to be negligible. From equations (B1), we have

$$u_g=-\frac{\partial_y p}{\rho f},\quad v_g=\frac{\partial_x p}{\rho f}. \tag{B13}$$

Therefore, averaged right-hand side of equation (B5) can be written as

$$\overline{-\frac{1}{\hat{\rho}}\partial_x p+f\left(\langle v\rangle+v'\right)}=\overline{-fv_g+fv}=\overline{fv_a}. \tag{B14}$$

Altogether, the averaged equation (B5) has the form

$$\begin{aligned}\partial_t\langle u\rangle=&-\frac{1}{A}\left[\int\left(\langle u\rangle^2+\left(u'\right)^2\right)\mathrm{d}y\right]_{x_1}^{x_2}\\&-\frac{1}{A}\left[\int\left(\langle u\rangle\langle v\rangle+u'v'\right)\mathrm{d}x\right]_{y_1}^{y_2}\\&-\frac{1}{A}\frac{1}{\hat{\rho}}\partial_z\iint\hat{\rho}u'w'\,\mathrm{d}x\,\mathrm{d}y+\overline{fv_a}.\end{aligned} \tag{B15}$$

The terms on the right-hand side can be divided into terms corresponding to the wave motion and terms corresponding to motions on larger scale. In particular, it is possible to identify three terms that add up to the zonal component of MWD,

$$MWD_{xx}=-\frac{1}{A}\left[\int\left(u'\right)^2\mathrm{d}y\right]_{x_1}^{x_2}, \tag{B16a}$$

$$MWD_{yx}=-\frac{1}{A}\left[\int u'v'\,\mathrm{d}x\right]_{y_1}^{y_2}, \tag{B16b}$$

$$MWD_{zx}=-\frac{1}{A}\frac{1}{\hat{\rho}}\partial_z\iint\hat{\rho}u'w'\,\mathrm{d}x\,\mathrm{d}y. \tag{B16c}$$

The quantity MWD_{xx} is the zonal derivative of the zonal flux of zonal wave momentum, MWD_{yx} is the meridional derivative of the meridional flux of zonal wave momentum and MWD_{zx} is the vertical derivative of the vertical flux of zonal wave momentum.

Analogously, for the meridional velocity component, it is possible to get equation

$$\begin{aligned}\partial_t \langle v \rangle = &-\frac{1}{A}\left[\int \left(\langle u \rangle \langle v \rangle + u'v'\right) \mathrm{d}y\right]_{x_1}^{x_2} \\ &-\frac{1}{A}\left[\int \left(\langle v \rangle^2 + (v')^2\right) \mathrm{d}x\right]_{y_1}^{y_2} \\ &-\frac{1}{A}\frac{1}{\hat{\rho}}\partial_z \iint \hat{\rho} v'w' \,\mathrm{d}x\,\mathrm{d}y - \overline{f u_a}.\end{aligned} \tag{B17}$$

We get terms of the meridional component of MWD,

$$MWD_{xy} = -\frac{1}{A}\left[\int u'v' \,\mathrm{d}y\right]_{x_1}^{x_2}, \tag{B18a}$$

$$MWD_{yy} = -\frac{1}{A}\left[\int (v')^2 \,\mathrm{d}x\right]_{y_1}^{y_2}, \tag{B18b}$$

$$MWD_{zy} = -\frac{1}{A}\frac{1}{\hat{\rho}}\partial_z \iint \hat{\rho} v'w' \,\mathrm{d}x\,\mathrm{d}y. \tag{B18c}$$

APPENDIX C

Algorithm for Cutoff Specification in Spectral Slope Method

Below we provide a programming language-neutral description of the structure of the algorithm for specification of cutoff in the spectral slope method:

```
Functions:
  adjacent_left(point) → returns the point in the log spectrum to the left of the given point
  adjacent_right(point) → returns the point in the log spectrum to the right of the given point
  fit_line(set of points) → returns the line fit error
  fit_line_slope(set of points, slope) → returns the line fit error with the given slope

algorithm(spectrum_plot) → maximal wavelength considered as GWs:
  λ1, E1 ← the leftmost point in plot
  λN, EN ← the rightmost point in plot
```

```
setL = {[λ1, E1]}
setR = {[λN, EN]}
λ1, E1 ← adjacent_right([λ1, E1])
λN, EN ← adjacent_left([λN, EN])
while (setL ∪ setR ≠ all points)
     fit_errL = fit_line(setL ∪ {[λN, EN]})
     fit_errR = fit_line_slope(setR ∪
                              {[λR, ER]}, -5/3)
     if (fit_errL < fit_errR):
         setL ← setL ∪ {[λL, EL]}
        λL, EL ← adjacent_right([λL, EL])
     else
        setR ← setR ∪ [λR, ER]
        λR, ER ← adjacent_left([λR, ER])
return max(setR)
```

References

Achatz, U., B. Ribstein, F. Senf, and R. Klein, 2017: The interaction between synoptic-scale balanced flow and a finite-amplitude mesoscale wave field throughout all atmospheric layers: weak and moderately strong stratification. *Quarterly Journal of the Royal Meteorological Society*, **143 (702)**, 342–361.

Alexander, M. J., and Coauthors, 2010: Recent developments in gravity-wave effects in climate models and the global distribution of gravity-wave momentum flux from observations and models. *Quarterly Journal of the Royal Meteorological Society*, **136 (650)**, 1103–1124.

Andrews, D. G., J. R. Holton, and C. B. Leovy, 1987: *Middle atmosphere dynamics*. Academic Press.

Bierdel, L., P. Friederichs, and S. Bentzien, 2012: Spatial kinetic energy spectra in the convection-permitting limited-area NWP model COSMO-DE. *Meteorologische Zeitschrift*, **21 (3)**, 245.

Blažica, V., N. Žagar, B. Strajnar, and J. Cedilnik, 2013: Rotational and divergent kinetic energy in the mesoscale model ALADIN. *Tellus A: Dynamic Meteorology and Oceanography*, **65 (1)**, 18 918.

Bramberger, M., and Coauthors, 2022: First super-pressure balloon-borne fine-vertical-scale profiles in the upper TTL: Impacts of atmospheric waves on cirrus clouds and the QBO. *Geophysical Research Letters*, **49 (5)**, e2021GL097 596.

Bühler, O., J. Callies, and R. Ferrari, 2014: Wave–vortex decomposition of one-dimensional ship-track data. *Journal of Fluid Mechanics*, **756**, 1007–1026.

Burgess, B. H., A. R. Erler, and T. G. Shepherd, 2013: The troposphere-to-stratosphere transition in kinetic energy spectra and nonlinear spectral fluxes as seen in ECMWF analyses. *Journal of the atmospheric sciences*, **70 (2)**, 669–687.

Cushman-Roisin, B., and J.-M. Beckers, 2011: *Introduction to geophysical fluid dynamics: physical and numerical aspects*. Academic press.

Damiens, F., F. Lott, C. Millet, and R. Plougonven, 2018: An adiabatic foehn mechanism. *Quarterly Journal of the Royal Meteorological Society*, **144 (714)**, 1369–1381.

Denis, B., J. Côté, and R. Laprise, 2002: Spectral decomposition of two-dimensional atmospheric fields on limited-area domains using the discrete cosine transform (DCT). *Monthly Weather Review*, **130 (7)**, 1812–1829.

Dörnbrack, A., 2021: Stratospheric mountain waves trailing across northern Europe. *Journal of the Atmospheric Sciences*, **78 (9)**, 2835–2857.

Dunkerton, T., 1978: On the mean meridional mass motions of the stratosphere and mesosphere. *Journal of Atmospheric Sciences*, **35 (12)**, 2325–2333.

Dunkerton, T., 1984: Inertia–gravity waves in the stratosphere. *Journal of Atmospheric Sciences*, **41 (23)**, 3396 – 3404, https://doi.org/10.1175/1520-0469(1984)041<3396:IWITS>2.0.CO;2, URL https://journals.ametsoc.org/view/journals/atsc/41/23/1520-0469_1984_041_3396_iwits_2_0_co_2.xml.

Eichinger, R., H. Garny, P. Šácha, J. Danker, S. Dietmüller, and S. Oberländer-Hayn, 2020: Effects of missing gravity waves on stratospheric dynamics; part 1: climatology. *Climate Dynamics*, **54 (5)**, 3165–3183.

Ern, M., L. Hoffmann, and P. Preusse, 2017: Directional gravity wave momentum fluxes in the stratosphere derived from high-resolution AIRS temperature data. *Geophysical Research Letters*, **44 (1)**, 475–485.

Ern, M., P. Preusse, M. J. Alexander, and C. D. Warner, 2004: Absolute values of gravity wave momentum flux derived from satellite data. *Journal of Geophysical Research: Atmospheres*, **109 (D20)**.

Errico, R. M., 1985: Spectra computed from a limited area grid. *Monthly weather review*, **113 (9)**, 1554–1562.

Fritts, D. C., and M. J. Alexander, 2003: Gravity wave dynamics and effects in the middle atmosphere. *Reviews of geophysics*, **41 (1)**.

Gage, K. S., and G. D. Nastrom, 1986: Theoretical interpretation of atmospheric wavenumber spectra of wind and temperature observed by commercial aircraft during GASP. *Journal of Atmospheric Sciences*, **43 (7)**, 729–740.

Gaßmann, A., 2019: Analysis of large-scale dynamics and gravity waves under shedding of inactive flow components. *Monthly Weather Review*, **147 (8)**, 2861–2876.

Geller, M. A., and J. Gong, 2010: Gravity wave kinetic, potential, and vertical fluctuation energies as indicators of different frequency gravity waves. *Journal of Geophysical Research: Atmospheres*, **115 (D11)**.

Gisinger, S., and Coauthors, 2017: Atmospheric conditions during the deep propagating gravity wave experiment (deepwave). *Monthly Weather Review*, **145 (10)**, 4249–4275.

Gonzalez, R. C., and R. E. Woods, 2008: *Digital image processing*. 3rd ed., Prentice Hall.

Gupta, A., T. Birner, A. Dörnbrack, and I. Polichtchouk, 2021: Importance of gravity wave forcing for springtime southern polar vortex breakdown as revealed by ERA5. *Geophysical Research Letters*, **48 (10)**, e2021GL092 762.

Holton, J., 2004: *An introduction to dynamic meteorology*. Elsevier Academic Press, Burlington, MA.

Kinoshita, T., and K. Sato, 2013: A formulation of unified three-dimensional wave activity flux of inertia–gravity waves and rossby waves. *Journal of the atmospheric sciences*, **70 (6)**, 1603–1615.

Klaver, R., R. Haarsma, P. L. Vidale, and W. Hazeleger, 2020: Effective resolution in high resolution global atmospheric models for climate studies. *Atmospheric Science Letters*, **21 (4)**, e952.

Krasauskas, L., B. Kaifler, S. Rhode, J. Ungermann, W. Woiwode, and P. Preusse, 2022: Oblique propagation of mountain waves to the upwind side of the andes observed by GLORIA and ALIMA during the SouthTRAC campaign. *Earth and Space Science Open Archive*, 37, https://doi.org/10.1002/essoar.10512325.1.

Krisch, I., and Coauthors, 2017: First tomographic observations of gravity waves by the infrared limb imager GLORIA. *Atmospheric Chemistry and Physics*, **17 (24)**, 14 937–14 953.

Kruse, C. G., and R. B. Smith, 2015: Gravity wave diagnostics and characteristics in mesoscale fields. *Journal of the Atmospheric Sciences*, **72 (11)**, 4372–4392.

Kruse, C. G., and R. B. Smith, 2018: Nondissipative and dissipative momentum deposition by mountain wave events in sheared environments. *Journal of Atmospheric Sciences*, **75 (8)**, 2721–2740.

Kruse, C. G., and Coauthors, 2022: Observed and modeled mountain waves from the surface to the mesosphere near the Drake Passage. *Journal of the Atmospheric Sciences*, **79**, 909–932, https://doi.org/10.1175/JAS-D-21-0252.1.

Lehmann, C., Y.-H. Kim, P. Preusse, H.-Y. Chun, M. Ern, and S.-Y. Kim, 2012: Consistency between Fourier transform and small-volume few-wave decomposition for spectral and spatial variability of gravity waves above a typhoon. *Atmospheric measurement techniques*, **5 (7)**, 1637–1651.

Lindborg, E., 1999: Can the atmospheric kinetic energy spectrum be explained by two-dimensional turbulence? *Journal of Fluid Mechanics*, **388**, 259–288.

Lindborg, E., 2015: A Helmholtz decomposition of structure functions and spectra calculated from aircraft data. *Journal of Fluid Mechanics*, **762**.

Lindzen, R. S., 1981: Turbulence and stress owing to gravity wave and tidal breakdown. *Journal of Geophysical Research: Oceans*, **86 (C10)**, 9707–9714.

Menchaca, M. Q., and D. R. Durran, 2019: The influence of gravity waves on the slope of the kinetic energy spectrum in simulations of idealized midlatitude cyclones. *Journal of the Atmospheric Sciences*, **76 (7)**, 2103–2122.

Mirzaei, M., A. R. Mohebalhojeh, C. Zülicke, and R. Plougonven, 2017: On the quantification of imbalance and inertia–gravity waves generated in numerical simulations of moist baroclinic waves using the WRF Model. *Journal of the Atmospheric Sciences*, **74 (12)**, 4241–4263.

Nastrom, G. D., and K. S. Gage, 1985: A climatology of atmospheric wavenumber spectra of wind and temperature observed by commercial aircraft. *Journal of the atmospheric sciences*, **42 (9)**, 950–960.

NCL, 2019: The NCAR Command Language (Version 6.6.2) [Software]. Boulder, Colorado: UCAR/NCAR/CISL/TDD, http://dx.doi.org/10.5065/D6WD3XH5.

Ostertagova, E., and O. Ostertag, 2016: Methodology and application of Savitzky-Golay moving average polynomial smoother. *Global J. Pure Appl. Math*, **12**, 3201–3210.

Plougonven, R., A. de la Cámara, A. Hertzog, and F. Lott, 2020: How does knowledge of atmospheric gravity waves guide their parameterizations? *Quarterly Journal of the Royal Meteorological Society*, **146 (728)**, 1529–1543.

Polichtchouk, I., T. G. Shepherd, and N. J. Byrne, 2018: Impact of parametrized nonorographic gravity wave drag on stratosphere-troposphere coupling in the northern and southern hemispheres. *Geophysical Research Letters*, **45 (16)**, 8612–8618.

Preusse, P., M. Ern, P. Bechtold, S. Eckermann, S. Kalisch, Q. Trinh, and M. Riese, 2014: Characteristics of gravity waves resolved by ECMWF. *Atmospheric chemistry and physics*, **14 (19)**, 10 483–10 508.

Procházková, Z., 2021: *On the internal gravity wave-atmospheric circulation interaction*. Charles University, Faculty of Mathematics and Physics, diploma thesis, available from: http://hdl.handle.net/20.500.11956/127720.

Sacha, P., A. Kuchar, R. Eichinger, P. Pisoft, C. Jacobi, and H. E. Rieder, 2021: Diverse dynamical response to orographic gravity wave drag hotspots—a zonal mean perspective. *Geophysical Research Letters*, e2021GL093305.

Saujani, S., and T. G. Shepherd, 2006: A unified theory of balance in the extratropics. *Journal of Fluid Mechanics*, **569**, 447–464.

Schoon, L., and C. Zülicke, 2018: A novel method for the extraction of local gravity wave parameters from gridded three-dimensional data: description, validation, and application. *Atmospheric Chemistry and Physics*, **18 (9)**, 6971–6983.

Shakespeare, C. J., A. H. Gibson, A. M. Hogg, S. D. Bachman, S. R. Keating, and N. Velzeboer, 2021: A new Open Source implementation of Lagrangian filtering: A method to identify internal waves in high-resolution simulations. *Journal of Advances in Modeling Earth Systems*, **13 (10)**, e2021MS002 616.

Skamarock, W. C., 2004: Evaluating mesoscale NWP models using kinetic energy spectra. *Monthly weather review*, **132 (12)**, 3019–3032.

Skamarock, W. C., C. Snyder, J. B. Klemp, and S.-H. Park, 2019a: Vertical resolution requirements in atmospheric simulation. *Monthly Weather Review*, **147 (7)**, 2641–2656.

Skamarock, W. C., and Coauthors, 2019b: A description of the advanced research WRF model version 4. *National Center for Atmospheric Research: Boulder, CO, USA*, 145.

Smith, R. B., J. D. Doyle, Q. Jiang, and S. A. Smith, 2007: Alpine gravity waves: Lessons from MAP regarding mountain wave generation and breaking. *Quarterly Journal of the Royal Meteorological Society: A journal of the atmospheric sciences, applied meteorology and physical oceanography*, **133 (625)**, 917–936.

Smith, R. B., and C. G. Kruse, 2017: Broad-spectrum mountain waves. *Journal of the Atmospheric Sciences*, **74 (5)**, 1381–1402.

Stephan, C. C., C. Strube, D. Klocke, M. Ern, L. Hoffmann, P. Preusse, and H. Schmidt, 2019: Gravity waves in global high-resolution simulations with explicit and parameterized convection. *Journal of Geophysical Research: Atmospheres*, **124 (8)**, 4446–4459.

Stephan, C. C., N. Žagar, and T. G. Shepherd, 2021: Waves and coherent flows in the tropical atmosphere: New opportunities, old challenges. *Quarterly Journal of the Royal Meteorological Society*, **147 (738)**, 2597–2624.

Stephan, C. C., and Coauthors, 2022: Atmospheric energy spectra in global kilometre-scale models. *Tellus Series A-Dynamic Meteorology and Oceanography*, **74**, 280–299.

Strube, C., P. Preusse, M. Ern, and M. Riese, 2021: Propagation paths and source distributions of resolved gravity waves in ECMWF-IFS analysis fields around the southern polar night jet. *Atmospheric Chemistry and Physics*, **21 (24)**, 18 641–18 668.

Sun, Y. Q., R. Rotunno, and F. Zhang, 2017: Contributions of moist convection and internal gravity waves to building the atmospheric- 5/3 kinetic energy spectra. *Journal of the Atmospheric Sciences*, **74 (1)**, 185–201.

Sundararajan, D., 2001: *The discrete Fourier transform: theory, algorithms and applications*. World Scientific.

951 Tange, O., and Coauthors, 2011: Gnu parallel-the command-line power tool. *The USENIX Maga-*
952 *zine*, **36 (1)**, 42–47.

953 Teixeira, M. A., 2014: The physics of orographic gravity wave drag. *Frontiers in Physics*, **2**, 43.

954 Teixeira, M. A. C., and B. Grisogono, 2008: Internal wave drag in stratified flow over mountains
955 on a beta plane. *Quarterly Journal of the Royal Meteorological Society: A journal of the*
956 *atmospheric sciences, applied meteorology and physical oceanography*, **134 (630)**, 11–19.

957 Vallis, G. K., 2017: *Atmospheric and oceanic fluid dynamics*. Cambridge University Press.

958 Van Niekerk, A., I. Sandu, and S. B. Vosper, 2018a: The circulation response to resolved versus
959 parametrized orographic drag over complex mountain terrains. *Journal of Advances in Modeling*
960 *Earth Systems*, **10 (10)**, 2527–2547.

961 Van Niekerk, A., I. Sandu, and S. B. Vosper, 2018b: The circulation response to resolved versus
962 parametrized orographic drag over complex mountain terrains. *Journal of Advances in Modeling*
963 *Earth Systems*, **10 (10)**, 2527–2547.

964 Viúdez, Á., 2012: Potential vorticity and inertia–gravity waves. *Geophysical & Astrophysical*
965 *Fluid Dynamics*, **106 (1)**, 67–88.

966 Watanabe, S., K. Sato, Y. Kawatani, and M. Takahashi, 2015: Vertical resolution dependence of
967 gravity wave momentum flux simulated by an atmospheric general circulation model. *Geosci-*
968 *entific Model Development*, **8 (6)**, 1637–1644.

969 Wright, C. J., and J. C. Gille, 2013: Detecting overlapping gravity waves using the S-Transform.
970 *Geophysical Research Letters*, **40 (9)**, 1850–1855.